

Deep Eddy Kinetic Energy in the Tropical Pacific From Lagrangian Floats

A. Delpech¹ , S. Cravatte¹ , F. Marin¹ , C. Ménesguen² , and Y. Morel¹ 

¹LEGOS (Laboratoire d'Etudes en Géophysique et Océanographie Spatiales), Université de Toulouse, CNES, CNRS, IRD, Toulouse, France, ²LOPS (Laboratoire d'Océanographie Physique et Spatiale), Université de Bretagne Occidentale, Ifremer, CNRS, IRD, Brest, France

Key Points:

- Eddy kinetic energy at 1,000 m in the tropical Pacific is investigated using Argo float drifts
- Deep intra-annual variability is evidenced with 30-day period and 1,000-km wavelength at the equator and 70-day period, 500 km off the equator
- Eddy kinetic energy exhibits small-scale features, suggesting interactions with the mean jet-like circulation at 1,000 m

Correspondence to:

A. Delpech,
audrey.delpech@legos.obs-mip.fr

Citation:

Delpech, A., Cravatte, S., Marin, F., Ménesguen, C., & Morel, Y. (2020). Deep eddy kinetic energy in the tropical Pacific from Lagrangian floats. *Journal of Geophysical Research: Oceans*, 125, e2020JC016313. <https://doi.org/10.1029/2020JC016313>

Received 9 APR 2020

Accepted 30 JUL 2020

Accepted article online 3 AUG 2020

Abstract At the ocean surface, satellite observations have shown evidence of a large spectrum of waves at low latitudes. However, very little is known about the existence and properties of the deep variability. Most of the subsurface observations rely on localized measurements, which do not allow for a global estimation of this variability. In this study, we use velocity estimates, provided by Argo float drifts at 1,000 m, to analyze the spatial and temporal distribution of the deep eddy kinetic energy (EKE) and its spectral signature with an unprecedented time and space coverage. In the tropical Pacific, high EKE is found along the equator, at the western boundary and poleward of 7°N. EKE meridional distribution is also found to vary at the scale of the meridionally alternating mean zonal jets: it is higher inside eastward currents. We develop an original statistical scale analysis to determine the temporal and spatial scale dependence of this deep EKE footprint. We show the presence of periodic features whose characteristics are compatible with theoretical equatorial waves dispersion relations. Annual and semiannual Rossby waves are observed at the equator, as well as ~30-day Yanai waves, consistent with surface tropical instability waves. The location and intensification of these waves match the downward energy propagation predicted by ray tracing linear theory. Short-scale variability (with ~70-day periods and 500-km wavelength) has also been detected poleward of 7°N. The generation mechanisms of this variability are discussed, as well as its potential importance for the mean circulation.

Plain Language Summary Energy in the deep ocean is important as it is a potential driver of the deep circulation, which has important climate feedbacks. Because of its singular dynamics, the equatorial ocean is a preferential region of transfer of energy from the surface to the interior of the ocean. Very little is known, however, about the energy content in the deep equatorial oceans. In this study, we use the large number of floats, called Argo floats, drifting at 1,000-m depth in the ocean to describe the deep kinetic energy in equatorial regions. We show that various energetic waves are present at 1,000 m in the tropical Pacific, and we discuss their potential generation mechanisms as well as their implications for the circulation. These new observations may help to validate some theories or numerical simulations of the deep equatorial and tropical circulation.

1. Introduction

The mean circulation at low latitudes is structured into intense eastward- and westward-flowing currents, called jets. At the surface, currents develop in response to the trade winds, namely, the westward North Equatorial Current (NEC) and South Equatorial Current (SEC) (Lagerloef et al., 1999) and the eastward North Equatorial Countercurrent (NECC). The eastward Equatorial Undercurrent (EUC) flows inside the thermocline and is confined along the equator (Wyrтки & Kilonsky, 1984) (see Figure 1 for a schematic in the Pacific).

Below the thermocline, our knowledge of the circulation is more recent. Thanks to the large number of Argo floats deployed since the beginning of the program in 2000, deep velocity estimates have been made available basin wide. Several studies have revealed the presence of strong eastward and westward jets, equatorward of 20° (e.g., Cravatte et al., 2012; Lebedev et al., 2007; Ollitraul & Colin de Verdière, 2014; Ollitraul et al., 2006; Qiu et al., 2013) and reaching depths of 2,000 m (Cravatte et al., 2017).

The deep zonal velocity has been shown to follow an annual cycle (Cravatte et al., 2012; Zanowski et al., 2019), especially close to the equator where a reversal of the jets is observed (Gouriou et al., 2006).

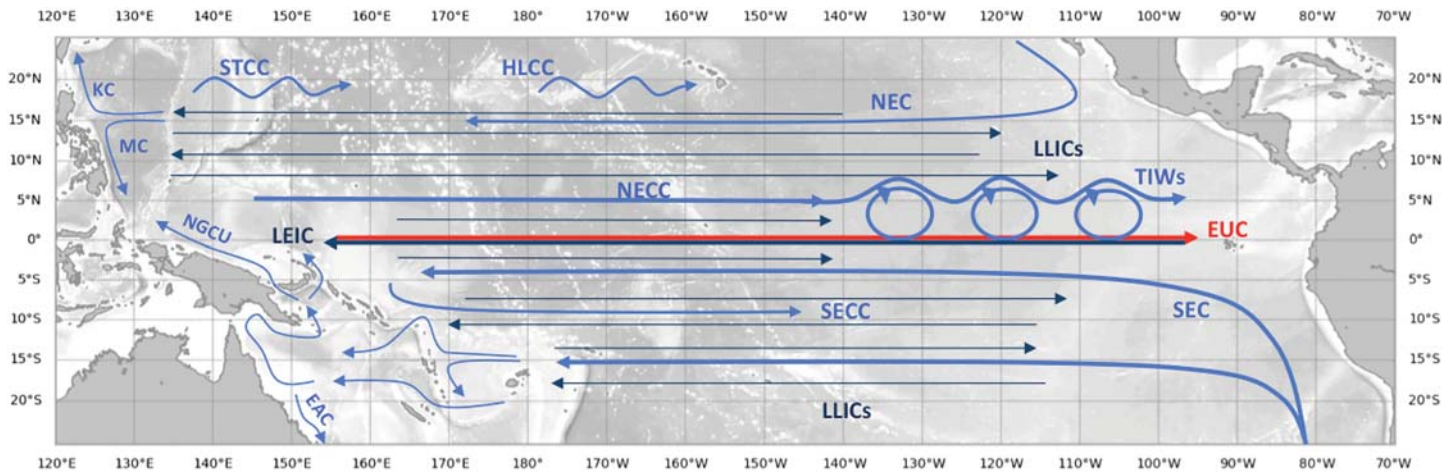


Figure 1. Schematics of the Pacific Ocean circulation. Light blue: surface currents, red: thermocline currents, deep blue: deep currents. EUC, Equatorial Undercurrent; HLCC, Hawaiian Lee Countercurrent; LEIC, Lower Equatorial Intermediate Current; LLICs, Low-Latitude Intermediate Currents; NEC, North Equatorial Current; NECC, North Equatorial Countercurrent; SEC, South Equatorial Current; SECC, South Equatorial Countercurrent; STCC, Subtropical Countercurrent; TIWs, tropical instability waves. Reproduced after Smith et al. (2019).

This has been attributed to the downward propagation of annual Rossby waves (Cravatte et al., 2012; Lukas & Firing, 1985; Marin et al., 2010). At inter-annual time scales, the zonal velocity at 1,000 m in the Pacific seems correlated to El Niño fluctuations with 6-month phase lag (Zanowski et al., 2019).

Understanding the energy sources and mechanisms at the origin of the deep jets remains a challenge. Several mechanisms have been proposed (see Ménesguen et al., 2019, for a review). Although they involve different physical processes, they all require an energy source in the deep ocean. Based on numerical simulations and theoretical considerations, several studies have shown that intra-annual waves at depth can provide this energy, driving a realistic deep circulation (Ascani et al., 2010, 2015; Bastin et al., 2020; Greatbatch et al., 2018; Hua et al., 2008; Ménesguen et al., 2009).

The variability in the equatorial regions is strong and has comparable amplitudes with the mean circulation. Intra-annual variability at depth could result either from a downward propagation of waves excited in the upper ocean, or could be generated directly at depth from instabilities of the strongest currents (like the deep western boundary current).

At the ocean surface, satellite-derived observations have revealed the presence of a broad spatial and temporal spectrum of waves at low latitudes (Lindstrom et al., 2014). Among the most energetic features are the tropical instability waves (TIWs), arising from the shear between the westward-flowing SEC and the eastward-flowing NECC and EUC (Philander, 1978). They develop along the temperature front at the border of the cold tongue in the eastern part of the basin (Figure 1) from July to November, when the temperature gradient is the highest (see Willett et al., 2006, for a review). They have been observed both in the Atlantic and Pacific oceans from satellite altimetry (Farrar, 2011; Legeckis, 1977; Lindstrom et al., 2014; Lyman et al., 2005, 2007, and references therein), but also in in situ meridional velocities (Lyman et al., 2007; McPhaden, 1996) and temperatures (Chelton et al., 2000; Contreras, 2002; McPhaden, 1996). In the Pacific, they have a signature at the equator and 5°N associated with periods of 17 and 30 days, respectively (Lyman et al., 2007).

However, observational evidence of deep intra-annual variability remains scarce. Most of the observations rely on sparse mooring measurements or cruise transects. Equatorial moorings data have evidenced a strong signature in meridional velocity at 30- to 50-day periods in the upper 600 m (Von Schuckmann et al., 2008, in the Atlantic) and in the range 20–90 days in the Pacific (Wang et al., 2016; Zhang et al., 2020). Deeper observations down to 3,000 m (e.g., Bunge et al., 2008; Tuchen et al., 2018, in the Atlantic, Eriksen & Richman, 1988, in the Pacific) also revealed the presence of intra-annual variability. This variability has been related to the downward propagation of mixed Rossby-gravity waves possibly generated by TIWs (Tuchen

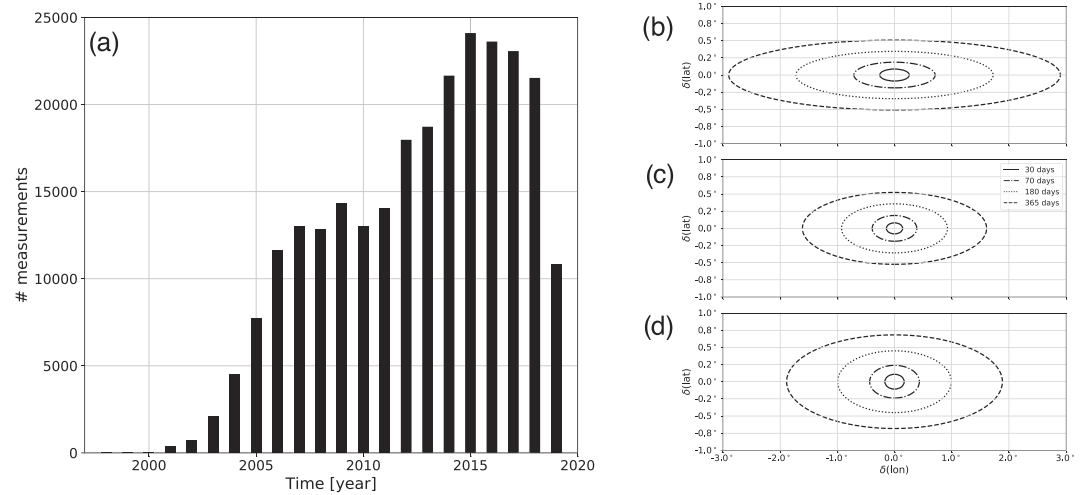


Figure 2. YoMaHA database statistics. (a) Number of 1,000-m velocity measurements per year in the tropical Pacific (update through August 2019). The 2014–2018 period corresponds to the most sampled period with a density exceeding 20,000 measurements per year. (b–d) Mean displacement $\delta(\text{lon})$, $\delta(\text{lat})$ of floats over different periods (30, 70, 180, and 365 days) in the different regions: (b) equatorial Pacific (west and east) 165°E to 90°W, 3°S to 3°N; (c) tropical Pacific (north and south), 170°E to 90°W, 7–17°S and N; and (d) western boundary 125°E to 135°W, 0–17°N.

et al., 2018). In addition, in the equatorial Pacific Ocean, Farrar and Durland (2012) have noted the presence of variability of surface dynamic height relative to 500 dbars, in the period range 5–15 days, associated with inertia-gravity and mixed Rossby-gravity waves. Along the western boundary in the equatorial Pacific, deep intra-annual variability has been attributed to the signature of strong subthermocline mesoscale eddies (Firing et al., 2005). However, the information provided by the moorings or cruise transects is very incomplete. It only gives a local estimate of the period or wavelength and does not allow for full characterization of scales. A global and more systematic assessment of this deep variability is still lacking.

In this study, we assess the variability in the deep tropical Pacific, with a focus on intra-annual periods. We aim to characterize its spectral range (both temporal and spatial) and variations at the basin scale. We will in particular address the following questions. (1) What are the amplitudes and characteristic (temporal and spatial) scales of the energy present at depth in the tropical Pacific? (2) Is there a spatial and temporal modulation of the observed signals? (3) Is there coherence of the signals that could be related to particular physical processes, such as wave or eddy propagation?

We address these questions by analyzing the fluctuations of the 10-day averaged Lagrangian velocity measured by the Argo float displacements at 1,000 m in the tropical Pacific. We develop statistical methods of scale analysis that extract information from these numerous and sparse velocity estimates. The relationship between the velocities measured at the same time between pairs of floats gives insight into the spatial scales of the dynamical structures. Similarly, the relationship between sequential measurements gives information on the temporal scales of these structures. In addition, combined spatial and temporal dependence can give information on the propagation of the signals. To be valid, a statistical analysis requires a critical number of data. This was made possible by the increasing number of Argo floats since the beginning of the program (Figure 2) and, in particular, by the seeding of hundreds of floats in the equatorial Pacific in 2014 (Roemmich et al., 2019). Given the temporal data sampling of the Argo program, this study focuses on periods from 20 days to annual.

The paper is organized as follows. Section 2 describes the data set and the statistical methods. Section 3 describes the spatial and temporal variations of the eddy kinetic energy (EKE) in the tropical Pacific and identifies some energetic regions. Then, in each identified region, the scale dependence of the energy content is analyzed. Section 4 discusses these results in the light of processes associated with propagating equatorial waves and their potential implication for the regional dynamics. Some limitations of our study are also identified along with suggestions for future research.

2. Data and Method

2.1. Database Description

The data used in this study are the deep velocity estimates from the displacements of Argo floats at their parking depth. These velocities are computed from the float drifts along their trajectories, estimated from the floats' differential surface positions fixed by satellite between each dive cycle. These estimates result in a series of nearly 10-day averaged Lagrangian deep velocities. These estimates include horizontal velocities measured when profiling from 0 to 2,000 m and back (about a half day out of every 10-day cycle). This source of uncertainty is usually small (around 0.4 cm s^{-1} in the tropical Pacific, see Cravatte et al., 2012 and Ollitrault & Rannou, 2013) and can be neglected on average.

We denote N as the total number of velocity estimates, N_i the total number of velocity estimates for the float i (corresponding to the number of dive cycles for the float i), and M the total number of floats, such that $\sum_{i=1}^M N_i = N$. For a given float i , we denote zonal and meridional velocities series respectively as $(U_n^i(x_n^i, y_n^i, t_n^i))_{n \in \{1..N_i\}}$ and $(V_n^i(x_n^i, y_n^i, t_n^i))_{n \in \{1..N_i\}}$, where x_n^i , y_n^i , and t_n^i are the mean longitude, latitude, and time for the dive cycle n , respectively.

The deep velocity estimates used are provided by the YoMaHA database updated through August 2019 (Lebedev et al., 2007). Although similar databases exist with perhaps more accurate velocity estimates (e.g., ANDRO from Ollitrault & Rannou, 2013), the YoMaHA database has been preferred in this study because it is nearly real-time updated and provides the densest coverage in our region of interest. The majority of the floats (63%) are programmed for a 1,000-m parking depth. In the remainder of this paper, we perform our diagnostics on the 1,000-m velocity estimates only by keeping floats whose parking depth is between 950 and 1,050 m. The other depths do not provide a sufficient coverage for a statistical approach and are discarded. Speeds in excess of 40 cm s^{-1} , found in 0.07% of the samples, were rejected as outliers. Some statistics about the number of floats and measurements of this data set available in the tropical Pacific, as well as the different regions considered in this study (section 3), are presented in Table 1 and Figure 2.

In the following, we consider either time series of velocity for each float i , $(U^i(t_n^i))_{n \in \{1..N_i\}}$, $(V^i(t_n^i))_{n \in \{1..N_i\}}$ (section 2.2.2), or series of independent velocity estimates, regardless of the float number, $(U_n, V_n)_{n \in \{1..N\}}$ (section 2.2.3).

2.2. Method

2.2.1. Energy Variables Definition

As the aim of this study is to characterize the deep variability, we perform a classical Reynolds decomposition of the velocity to separate the mean and the variable part of the flow:

$$\begin{cases} U(x, y, t) = \bar{U}(x, y) + U'(x, y, t) \\ V(x, y, t) = \bar{V}(x, y) + V'(x, y, t) \end{cases} \quad (1)$$

where the overbar indicates the time average for the whole period 1997–2019 and the prime the fluctuations with respect to this average.

We define the mean kinetic energy (MKE) and EKE at any given location x, y as twice the kinetic energy per unit mass contributed by their respective velocity components:

$$\begin{aligned} \text{MKE}_q(x, y) &= \overline{q(x, y, t)^2} = \bar{q}(x, y)^2 \\ \text{EKE}_q(x, y) &= \overline{q'(x, y, t)^2} \\ &= \overline{(q(x, y, t) - \bar{q}(x, y))^2} \end{aligned} \quad (2)$$

where $q = (U_n)_{n \in \{1..N\}}$ or $q = (V_n)_{n \in \{1..N\}}$.

Previous studies have shown that the annual cycle is the dominant mode of variability of the 1,000-m zonal currents in the equatorial region (Cravatte et al., 2012). In order to estimate the other periods of variability, we define U^* as the zonal velocity where the monthly climatology has been filtered out.

Table 1

YoMaHA Database Statistics of 1,000-m Velocity Estimates in the Tropical Pacific Basin for the Whole Argo Period 1997–2019

	# Floats	# Measurements	Avg. lifetime (days)	Avg. x-dist (° lon)	Avg. y-dist (° lat)	# Synchron.	# Clim.
Trp. Pacific	1,879	256,139	1,416	16.5	4.0	179	19,994
EW	172	8,237	656	13.9	1.9	7	405
EE	267	21,278	903	15.5	2.2	18	1,236
TS	451	46,079	1,160	11.6	2.5	34	1,233
TN	402	45,782	1,325	15.6	3.3	35	1,009
WB	89	7,735	755	9.2	4.2	9	142

Note. Trp. Pacific: 120°E to 70°W, 20°S to 20°N. EW: 165°E to 175°W, 3°S to 3°N. EE: 155°W to 90°W, 3°S to 3°N. TN: 170°E to 125°W, 7°N to 17°N. TS: 160°W to 90°W, 7°S to 17°S. WB: 125°E to 135°E, 0° to 17°N (Figure 4). The average lifetime (avg. lifetime) represents the averaged time spent by each float in a given region. The average x-distance (avg. x-dist) and (avg. y-dist) y-distance represent the averaged maximal zonal and meridional extension of each float trajectory in a given region. The number of synchronous measurements (# synchron.) represents the mean number of measurements in the region per time intervals of 10 days, and the number of climatological measurements (# clim.) represents the minimal number of measurements per climatological month used to construct the U^m field (Equation 3).

$$U^*(x, y, t) = U(x, y, t) - U^m(x, y, t) \quad (3)$$

where the superscript m refers to the monthly climatology of U . The associated EKE is

$$EKE_U^*(x, y) = \overline{U^*(x, y, t)^2} \quad (4)$$

EKE_U^* thus contains both the intra-annual and inter-annual components of the zonal velocity fluctuations.

In practice, $(U_n)_{n \in \{1..N\}}$ and $(V_n)_{n \in \{1..N\}}$ are unstructured fields: position and time change for each measurement, and there are no repeated measurements at any location. The time-averaged fields \bar{U} , \bar{V} , and U^m are

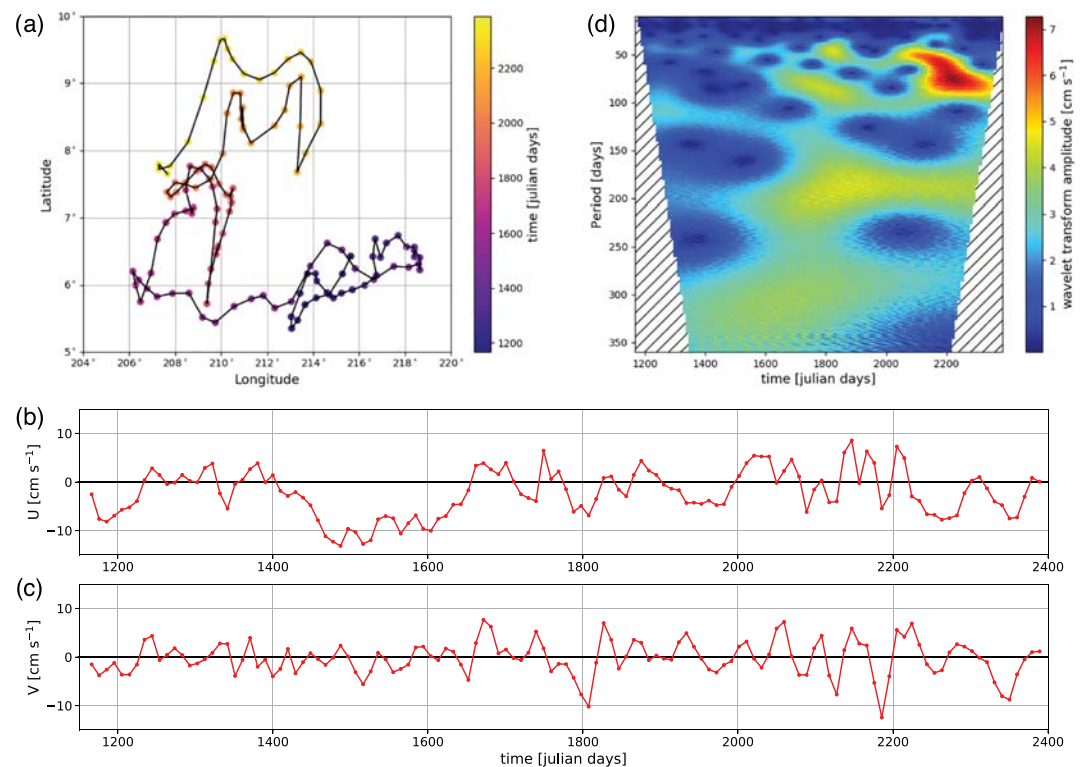


Figure 3. (a) Example of an individual float trajectory as a function of time (color scale) from the YoMaHA database (float N°3557), (b) float U time series, (c) float V time series, and (d) wavelet analysis of the V time series. The dashed area indicates the cone of influence; in this area, the estimations are biased by edge effects and are thus not considered.

thus obtained from a gridding method. Here we use optimal interpolation of the fields from Cravatte et al. (2012). The EKE field is then computed from a simple binned average with a bin size of $1^\circ \times 1^\circ$.

Following Roulet et al. (2014), we define the eddy available potential energy (EAPE) as

$$\text{EAPE}(x, y) = -\frac{g}{2\rho_0} \overline{\zeta'(x, y)\rho'(x, y)} \quad (5)$$

where ζ' is the vertical isopycnal displacement and ρ' the density anomaly associated with this displacement. The EAPE used in this study comes from the data set (Roulet, 2020). The EAPE has been computed for each Argo profile (0–2,000 m) at 63 vertical levels and binned on a $0.25^\circ \times 0.25^\circ$ horizontal grid. In this study, we extracted the 1,000-m level. Outliers exceeding one standard deviation have been discarded. This corresponds to 1.3% of the data.

2.2.2. Estimation of Dominant Periods of Variability from Wavelet Transform

The dominant period is computed from the deep velocity time series associated with each individual float trajectory (e.g., Figures 3a to 3c). A continuous wavelet transform using a complex Morlet wavelet with periods from 10 to 450 days and a 1-day increment is performed on these time series (Lee et al., 2019). This method results in a local estimation of the amplitude of the signal at each frequency (Figure 3d). Note that it is not possible to estimate the wavelet transform for all periods near the beginning or the end of the time series, where edge effects potentially contaminate the signal (Torrence & Compo, 1998). Periods within this cone of influence are not considered (Figure 3d). For each measurement time (or equivalently position), the period with the largest amplitude, A_n , is selected as the dominant period P_n . Amplitude-weighted histograms of dominant periods, H_Ω , are then constructed in a given region Ω of the (x, y) plane, following Equation 6:

$$H_\Omega(p, p + dp) = \frac{1}{N_\Omega} \left(\sum_{\substack{(x_n, y_n) \in \Omega \\ p < P_n < p + dp}} A_n \right) \quad (6)$$

where p is a given period and dp an increment. Here, we use p going from 10 to 450 days, with $dp=10$ days. N_Ω is the total number of measurements in the region of consideration. Note that this method retains only the most energetic frequency, regardless of the energy present at other frequencies.

Four approximations are made for the computation of the dominant period.

First, we consider the velocity from the float time series as a real time series made of instantaneous velocities, while the velocity estimates given by the Argo product are ~ 10 -day averaged Lagrangian velocities along float trajectories. This will filter out signals with periods shorter than 10 days. In addition, the time series has a 10-day sampling rate following the Argo cycle. The corresponding Nyquist frequency is one cycle per 20 days. Aliasing of higher frequencies is reduced but not eliminated by the 10-day averaging.

Second, we neglect the Lagrangian character of the measurements and take the velocity time series as an Eulerian time series. This assumption is valid as long as the distance traveled by the float during the estimated wave period is short with respect to the wavelengths of the waves. The mean displacement of the floats increases with the estimated period and is maximal in the equatorial regions (Figures 2b to 2d). It reaches 1.5° longitude and 0.5° latitude at intra-annual periods (typically 70 days) and 6° longitude and 1° latitude at annual periods. The zonal displacements are short compared to the wavelengths derived from the equatorial wave dispersion relations ranging from a few hundreds of kilometers at intra-annual periods to thousands of kilometers at annual periods. Likewise, the meridional displacements remain shorter than the equivalent meridional wavelength of the equatorial waves (which are trapped within a few degrees of the equator).

Third, we neglect the Doppler shift. In presence of a mean flow, the apparent period of the wave is indeed modified (e.g., Barbot et al., 2018). This effect is stronger as the mean flow approaches the phase speed of the wave (see Appendix A).

Fourth, we neglect the Stokes drift, a nonlinear advection of a particle in a wave motion, directed along the phase speed of the wave. It is generally weak (Weber, 2017) and is assumed to be negligible with respect to the mean currents.

As shown in the next sections, these approximations are validated a posteriori by the consistency of our results with other diagnostics.

2.2.3. Statistical Scale Analysis

One of the aims of this study is to determine the scale dependence associated with the deep EKE footprint. Classical spectral analyses, including Fourier transforms, generally require uniformly sampled data. This condition is difficult to achieve with in situ observations unless applying interpolation preprocessing. Moreover, such methods can introduce significant errors, in particular when data are scarce. We thus develop in this study a metric that measures both the spatial and temporal scale dependence of the horizontal velocity anomalies from the unstructured Argo measurements.

This metric has been largely inspired by structure functions (Babiano et al., 1985; Sérazin et al., 2020), developed to compute the scale dependence of kinetic energy from irregular data sampling (Morel & Larcheveque, 1974). They have been successfully applied to Lagrangian float measurements to study turbulent energy cascades (Balwada et al., 2016; McCaffrey et al., 2015). Most of the studies using structure functions, however, assume homogeneous, stationary, and isotropic flow statistics. These assumptions seem reasonable for midlatitude fully developed turbulence regimes but not for low-latitude wave-dominated regimes.

We define the statistical scale function (SSF) as the mean squared difference between quantities at points separated by a given distance and time laps. Because it considers both space direction and time separations, SSF accounts for the anisotropy of the flow and captures propagating patterns. It still assumes a statistical stationarity (the spectral characteristics of the variability do not evolve in time).

Denoting δq as the increment of a quantity q between two independent measurements (i, j) with positions \vec{x}_i and \vec{x}_j and time t_i and t_j ,

$$\delta q(\vec{x}_i, t_i, \vec{x}_j, t_j) = q(\vec{x}_j, t_j) - q(\vec{x}_i, t_i) \quad (7)$$

Under the assumption of homogeneity (the statistics do not depend on space and time in the region of focus), we define the SSF D_q of a quantity q as

$$D_q(\vec{dx}, dt) = \frac{1}{n_{ij}\{i, j\}} \sum_{\substack{\vec{x}_j - \vec{x}_i = \vec{dx} \\ t_j - t_i = dt}} \delta q(\vec{x}_i, t_i, \vec{x}_j, t_j)^2 \quad (8)$$

where \vec{dx} and dt are given separation vector and time lapse and $\{i, j\}$ are the possible pairs of measurements that satisfy the condition $\vec{x}_j = \vec{x}_i + \vec{dx}$ and $t_j = t_i + dt$, with n_{ij} the number of such pairs. $D_q(\vec{dx}, dt = 0)$ corresponds exactly to the second-order structure function of the quantity q .

Here, q is taken as U, V for the zonal and meridional components of the velocity. In addition, we generally only take into account the zonal component of the separation scale ($\vec{dx} = dx \vec{i}$) as we mostly expect zonal propagation and will simply write $D_q(dx, dt)$. Taking the full separation vector ($\vec{dx} = dx \vec{i} + dy \vec{j}$) would considerably reduce the number of pairs available at a given separation scale and would not lead to robust statistics.

As a consequence, computing SSF assumes homogeneous variables along the meridional direction. For this assumption to be valid, we apply this metric in regions where we expect homogeneity (section 3.3). Tests have shown that our results are not particularly sensitive to the borders of the regions within which we calculate SSF.

The separation scales, dx, dt , of the increments are binned on a $0.5^\circ \times 5$ days grid, yielding at least 100 pairs by bin. The size of the bins used for the gridding directly determines the scales that are resolved for dx and dt .

Assuming that the effective resolution is approximately 3 times the grid resolution, the chosen grid resolves scales $dx > 1.5^\circ$ and $dt > 15$ days. Given the time series length and the region dimensions, periods longer than 9 years and zonal wavelengths shorter than 160° are filtered out. In order to avoid large noise, only scales (dx, dt) for which the number of measurements is greater than 100 are considered.

As an example, we consider the ideal case of a velocity field corresponding to a plane wave propagating along the x direction. The wave is associated with the following velocity field:

$$\begin{cases} u(x, t) = 0 \\ v(x, t) = v_0 \sin(k_0 x - \omega_0 t) \end{cases} \quad (9)$$

It can be shown that the SSF is equal to zero along the phase line of the wave. Denoting c_0 as the phase speed of the wave $\left(c_0 = \frac{\omega_0}{k_0}\right)$, the phase lines are defined by the equation $dx = c_0 dt$, and

$$D_v(c_0 dt, dt) = \frac{1}{n_i} \sum_i \left[v_0 \sin(k_0 x_i - \omega_0 t_i) - v_0 \sin\left(k_0 \left(x_i + \frac{\omega_0}{k_0} dt\right) - \omega_0(t_i + dt)\right) \right]^2 = 0 \quad (10)$$

In particular, the SSF is equal to zero when the separation distance is equal to the wavelength and $dt = 0$ or when the time difference is equal to the period of the wave and $dx = 0$:

$$\begin{cases} D_v\left(0, \frac{2\pi}{\omega_0}\right) = 0 \\ D_v\left(\frac{2\pi}{k_0}, 0\right) = 0 \end{cases} \quad (11)$$

The amplitude of the wave can be estimated from the amplitude of the SSF along its maximal amplitude lines (where either the distance is equal to the half wavelength or the time lags is equal to the half period of the wave):

$$D_v\left(\frac{2\pi}{2k_0}, 0\right) = \frac{1}{n_i} \sum_i \left[v_0 \sin(k_0 x_i - \omega_0 t_i) - v_0 \sin\left(k_0 \left(x_i + \frac{2\pi}{2k_0} dt\right) - \omega_0 t_i\right) \right]^2 \quad (12)$$

$$= 4v_0^2 \frac{1}{n_i} \sum_i \sin^2(k_0 x_i - \omega_0 t_i) = 2v_0^2 \quad (13)$$

assuming that (x, t) is uniformly randomly sampled and therefore that $\frac{1}{n_i} \sum_i \sin^2(k_0 x_i - \omega_0 t_i) = \frac{1}{2}$.

In practice, the velocity is unlikely to be a pure wave field and velocities available from the Argo data set are not instantaneous Eulerian velocities but averaged Lagrangian velocities. So we do not expect the SSF to be equal to zero at the scales corresponding to the wavelength and wave period, but rather to reach a minimum, and we expect the amplitude of the SSF to be underestimated. Similarly, if (x, t) is not uniformly sampled, the SSF at the half period and half wavelength may depart from the theoretical formula given in Equation 13. In addition, the waves might be dissipated, or wavetrains with different phases might coexist and will reduce the coherence of the SSF signal at large dx and dt . The signature of the dominant wave, if any, will thus more likely stand out for space time separation within a few wavelengths or periods near the origin ($dx = 0, dt = 0$).

This method has been validated by advecting synthetic floats within a prescribed wave field and by controlling that the estimated wavelength and period match the prescribed ones (see Appendix B). Figure B1 gives the typical SSF pattern if a wave signal dominates the dynamics. Given the limits of the method discussed above, we expect the amplitude to be generally underestimated. There are, however, fewer approximations with this method than with wavelet transforms described in section 2.2.2.

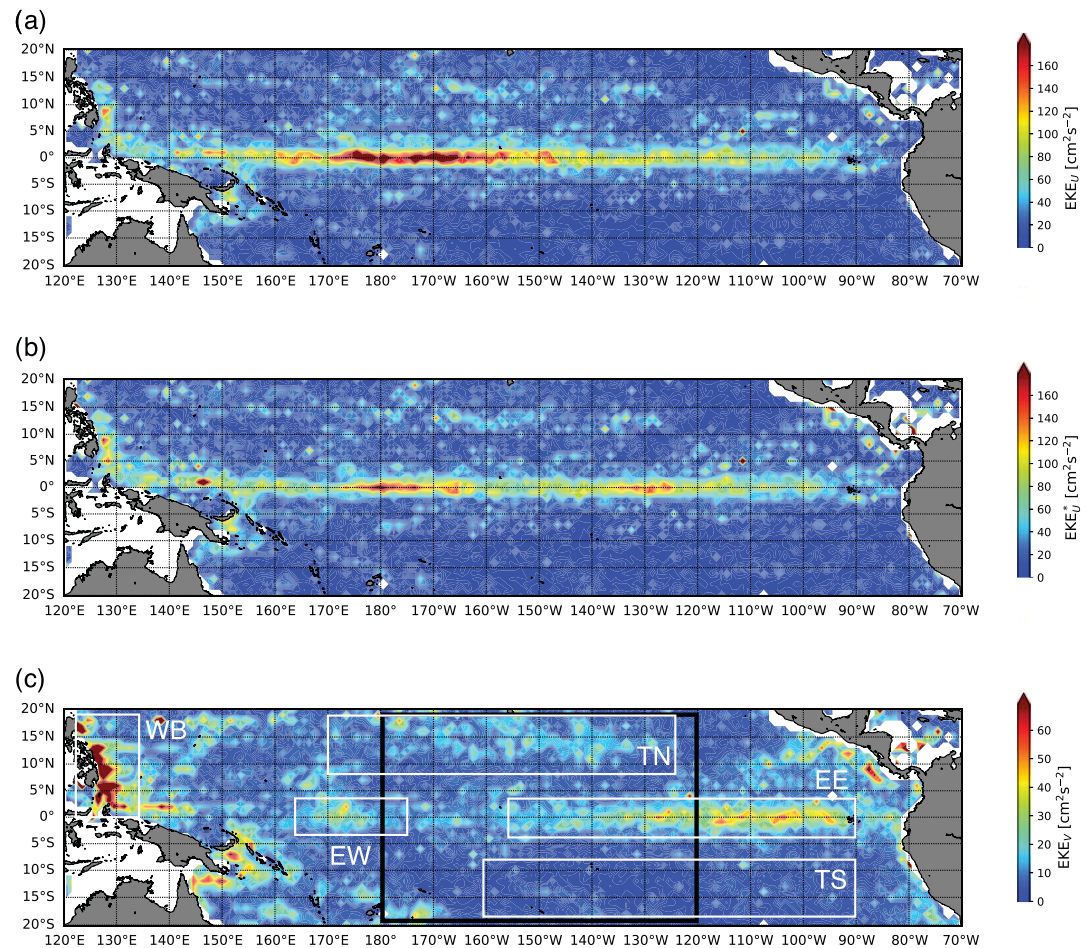


Figure 4. Map of (a) EKE_U , (b) EKE_U^* (corresponding to the EKE associated with the zonal component of the velocity for which the mean annual cycle has been filtered out), and (c) EKE_V computed from the 1,000-m velocity anomalies and binned on a $1^\circ \times 1^\circ$ horizontal grid over the period 1997–2019.

3. Results

3.1. Deep EKE in the Tropical Pacific

3.1.1. Inhomogeneity of the Spatial Distribution of EKE

The deep (1,000 m) zonal EKE (EKE_U) is spatially inhomogeneous. It is larger at the equator, especially in the 170°E to 160°W longitude range where it can reach up to $200 \text{ cm}^2 \text{ s}^{-2}$ (Figures 4a and 5a). Part of this signal can be attributed to the annual variability, which is strong at the equator and decreases poleward to 8° (Cravatte et al., 2012). Once the mean annual cycle is filtered out, the residual EKE (EKE_U^*) containing the intra- and inter-annual variability still shows a maximum along the equator, although its amplitude is reduced to $170 \text{ cm}^2 \text{ s}^{-2}$, and the western part (170°E to 160°W) of the signal has been considerably reduced (Figure 4b). A second relative EKE_U maximum ($\sim 40 \text{ cm}^2 \text{ s}^{-2}$) also shows up north of the equator (10°N to 17°N), while the Southern Hemisphere ($<5^\circ\text{S}$) exhibits a very weak EKE_U ($<10 \text{ cm}^2 \text{ s}^{-2}$).

The deep (1,000 m) meridional EKE (EKE_V) also has an heterogeneous regional distribution. The dominant signal ($>100 \text{ cm}^2 \text{ s}^{-2}$) is found along the western boundary (Figure 4c). The EKE_V is also larger at the equator, with distinct maxima in the western part ($\sim 170^\circ\text{E}$ to 170°W) and in the eastern part ($\sim 130^\circ\text{W}$ to 110°W) of the basin (Figure 4c). A relatively large amount ($\sim 30 \text{ cm}^2 \text{ s}^{-2}$) of EKE_V is also found in the northern part of the basin (10°N to 17°N) (Figures 4c and 5b), while the EKE_V in the Southern Hemisphere is concentrated around the many islands, west of 170°W (Figure 4c).

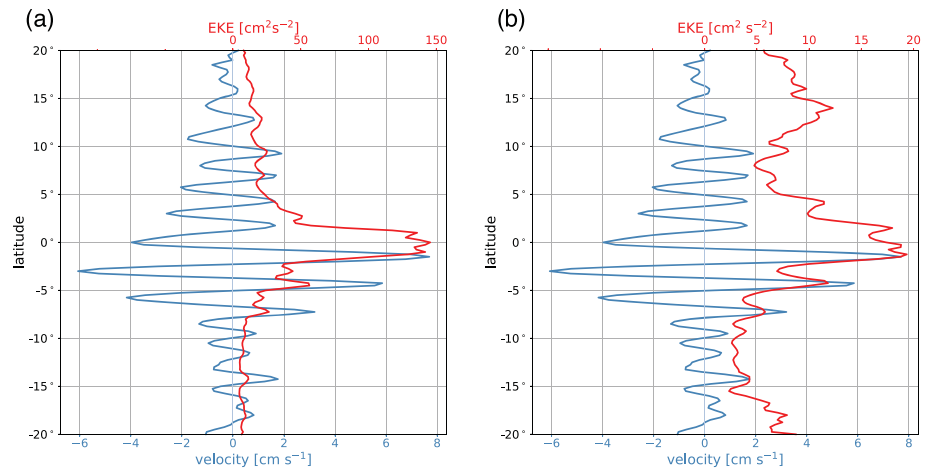


Figure 5. Mean zonal velocity $\bar{U}(y)$ (blue) and (a) EKE_U and (b) EKE_V (red) at 1,000 m averaged from 180° to 120°W (black box shown in Figure 4) over the period 1997–2019.

Superimposed on this large regional scale distribution of zonal and meridional EKE, variations of the amplitude are also observed at small meridional scales (Figures 5a and 5b), with zonally coherent, meridionally alternating maxima and minima of EKE. When compared to the structure of the meridionally alternating mean zonal velocities (Cravatte et al., 2012, blue curve in Figure 5), local EKE maxima are found to coincide with eastward jets and local EKE minima with westward jets equatorward of 15°. EKE_U local maxima are also observed in westward jets at 4°S and 7°S though.

Based on these results, we define five regions in which we analyze the characteristics of the large-scale EKE distribution in the following sections 3.2 and 3.3: the eastern equatorial region (EE: 155°W to 90°W, 3°S to 3°N), the western equatorial region (EW: 165°E to 175°W, 3°S to 3°N), the north tropical Pacific (TN: 170°E to 125°W, 7°N to 17°N), the south tropical Pacific (TS: 160°W to 90°W, 7°S to 17°S), and the western boundary region (WB: 125°E to 135°E, 0° to 17°N) (Figure 4c). The small-scale (jet-scale) EKE distribution is investigated in section 3.4.

3.1.2. Annual Modulation of the EKE

A monthly climatology of the EKE shows that some regions undergo an annual intensification of the EKE. This is the case in particular in EE region, where stronger EKE_V (up to 35 $\text{cm}^2 \text{s}^{-2}$) is observed in boreal autumn and winter (September to February) (Figure 6a). Similarly, in the TN region, EKE_V increases from 10 to 15 $\text{cm}^2 \text{s}^{-2}$ between June and December. Although it is less pronounced, the EW region also follows the same annual cycle, with an increase of EKE_V from 15 to 17–20 $\text{cm}^2 \text{s}^{-2}$ between May and December–January. The EKE_U at the equator also presents annual intensification mostly during spring and summer times (Figure 6b). In the EW region, EKE_U increases to 225 $\text{cm}^2 \text{s}^{-2}$ between June and September.

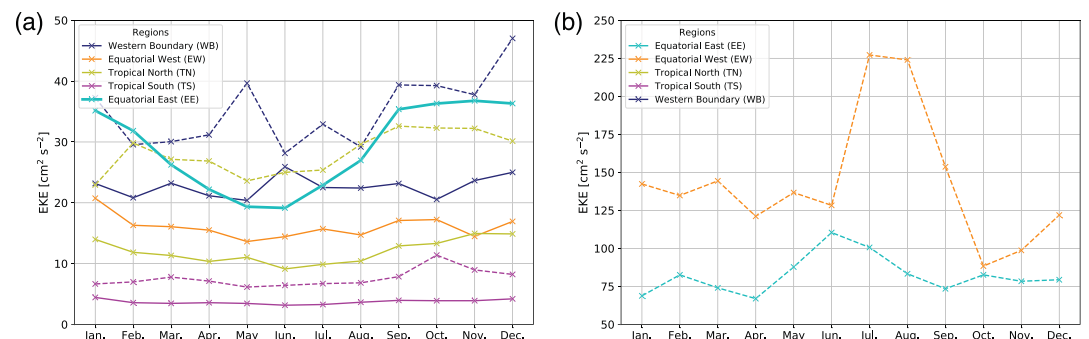


Figure 6. Monthly climatology (average from the first day to the last day of each month) of the EKE_U (dashed) and EKE_V (solid) in the different regions (colors) zoomed between (a) 0–50 and (b) 50–250 $\text{cm}^2 \text{s}^{-2}$.

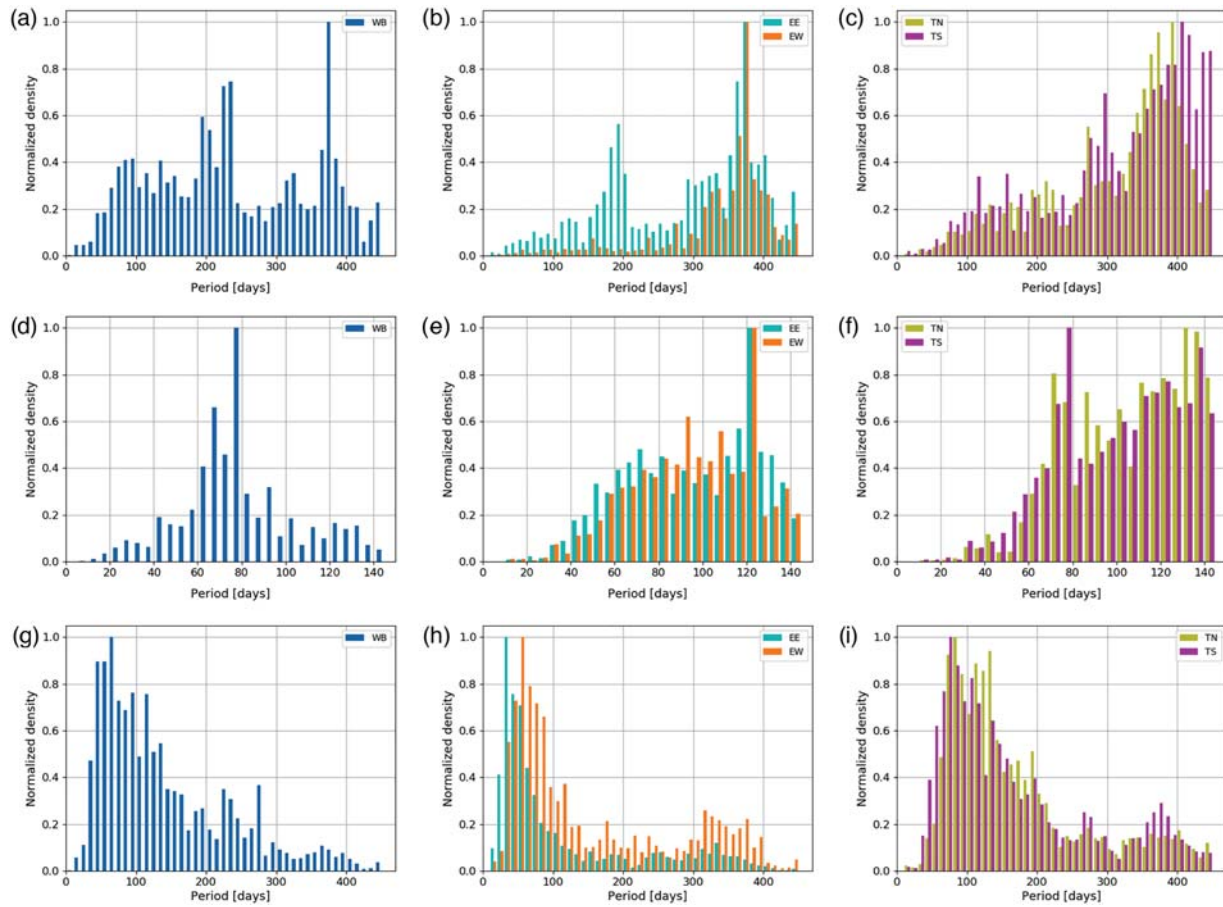


Figure 7. Periodograms for U' (top), U^* (middle), and V' (bottom) at the western boundary (left), in the equatorial regions (middle), and in the extra-equatorial regions (right). The periodograms are computed from wavelet analysis as $\frac{H}{H_{max}}$, where H follows Equation 6. It is computed for periods from 10 to 450 days with 10-day increments for U' and V' and from 10 to 145 days with 5-day increments for U^* .

EE region, EKE_U is intensified (up to $120 \text{ cm}^2 \text{ s}^{-2}$) between May and August (Figure 6b). Conversely, TS and WB regions do not present any climatological annual variations.

3.2. Dominant Periods of Variability

This section investigates the temporal scales (periods) associated with the velocity anomalies (U' , V' , and U^*) in the different regions identified in section 3.1. Figure 7 shows the dominant periods in the different regions from the amplitude-weighted histograms, as described in section 2.2.2.

The zonal velocity U' is mostly associated with long periods (>150 days). The equatorial region (EW and EE) shows a dominant annual period of ~ 360 days, that can be associated with the well-documented vertically propagating annual Rossby wave (Figure 7b) (Kessler & McCreary, 1993; Marin et al., 2010). In addition, the EE region has energy at semiannual period. Off-equatorial regions (TN and TS) have peak energy amplitude in the 350- to 380-day period range (Figure 7c). When filtering out the mean annual cycle (U^*) and focusing on the intra-annual variability, a dominant period of 120 days is found at the equator (Figure 7e) and an energy peak is found in the period range of 60–80 days in the WB region and around 75 days in TN and TS regions (Figures 7d and 7f, respectively).

Conversely, the meridional velocity V' is dominated by intra-annual periods (<150 days) in all regions. Dominant periods of 30 days are found in the EE region (Figure 7h), 50-day periods in the WB and EW regions (Figures 7g and 7h), and ~ 75 -day periods in the TN and TS regions (Figure 7i).

As explained in section 2.2.2, this method retains the dominant period, but variability at other periods may be present too. In particular, this could explain why maxima of U' and V' variability are not found in the

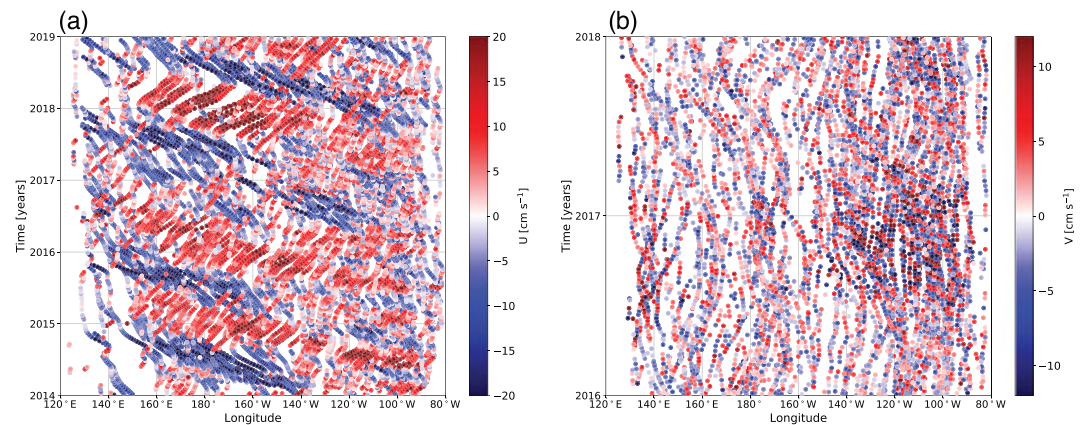


Figure 8. Hovmöller diagram of (a) zonal (U) and (b) meridional (V) 1,000-m velocities along the equator, within the latitude range 2°S to 2°N .

same period ranges. The two variables are the dominant signature of different variability sources. It is, however, interesting to notice the similarity between U^{*} and V' . Both variables have intra-annual variations with a dominant period around 75 days off the equator.

3.3. Regional Statistical Scale Analysis

Hovmöller diagrams of the zonal and meridional velocity anomalies estimated from individual floats along given latitudes (e.g., along the equator in Figure 8) show an organization of the positive and negative anomalies of the velocity into tilted lines, consistent with westward propagation of waves or eddies

The period and wavelength can be estimated as the interval between two anomalies of the same sign on the y axis and x axis, respectively. The zonal velocity is associated with longer periods and wavelengths (around 1 year and several thousands of kilometers) (Figure 8a) than the meridional velocity (few days and few degrees) (Figure 8b). In addition, zonal and meridional velocities do not share constant periods, wavelengths, and amplitudes across the basin. The zonal velocity has longer periods (~ 1 year) in the western part (west of 220°) than in the eastern part of the basin (around half a year east of 220°E) (Figure 8a). The meridional velocity shows a clearer pattern of phase lines east of 180° , where the amplitude of the velocity is also larger ($>10 \text{ cm s}^{-1}$).

Although the Hovmöller diagram already determines the period and wavelength associated with the observed anomalies, it presents some limitations. First, it requires a large number of measurements concentrated in some longitude time intervals. This requirement is met only in certain regions such as the eastern equatorial Pacific. Second, the short scales are difficult to capture with this method (e.g., Figure 8b).

These reasons led us to develop the statistical scale analysis approach presented in section 2.2.3. This approach no longer considers the time and position of each observation but rather the time difference and the distance between pairs of observations. This takes better advantage of all available information, leading to a more robust estimation. In the remainder of this section, the temporal and spatial characteristics of the velocity components are investigated in each region defined in Table 1 and Figure 4c using the SSF described in section 2.2.3.

3.3.1. Western Equatorial Pacific

The $\text{SSF}_{U'}$ in the EW region shows three relative minima and two relative maxima along tilted lines (Figure 9a). A minimal amplitude of the SSF is associated with a maximal phase correlation with respect to the origin. The time lags dt and distance dx at which SSF is minimal are multiples of the period and wavelength (section 2.2.3). The period can be easily estimated by finding where minimal lines cross the $dx = 0$ axis. This is found for $dt = 0$, $dt = 380$, and $dt = 720$, giving a period estimate of around 360 days. The half wavelength can be estimated by extending the first maximum line until reaching the $dt = 0$ axis. This gives $dx = 70^{\circ}$ a wavelength estimate of about 140° . The estimated phase speed is 0.5 m s^{-1} . In the WE region, the zonal velocity anomalies thus show a westward-propagating signal at an annual period and a basin-scale

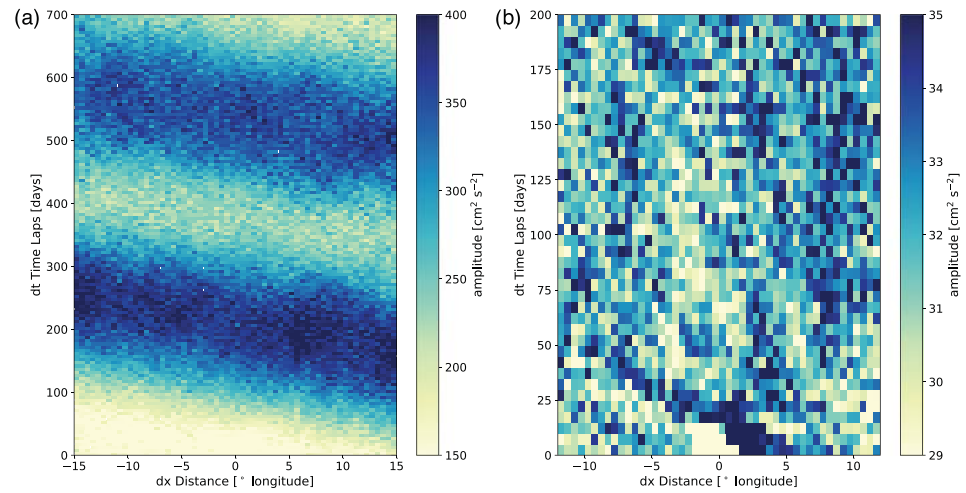


Figure 9. SSF for (a) U' and (b) V' at 1,000-m depth in the box EW of Figure 4. All grid cells contain at least 100 realizations.

wavelength ($\sim 140^\circ$), coherent over at least 2 years and 15° longitude (Figure 9a). This confirms the importance of the annual cycle in this region, taking the form of a Rossby wave, as shown by Cravatte et al. (2012). The amplitude of the SSF $_{U'}$ is $400 \text{ cm}^2 \text{ s}^{-2}$, which corresponds to a wave amplitude of 10 cm s^{-1} (section 2.2.3), also compatible with Cravatte et al. (2012). The meridional velocity anomalies also show a westward-propagating signal with a smaller phase speed (0.2 m s^{-1}) and a shorter period (50 days) and wavelength ($\sim 750 \text{ km}$) (Figure 9b). In addition, the signal amplitude (3.2 cm s^{-1}) and coherence (<100 days and $<10^\circ$) are much weaker than the ones for the zonal velocity. This can be caused for example by a time modulation of the source, or by the presence of a strong vertical component of propagation.

Zonal and meridional EKE period estimates from the SSF are consistent with those from section 3.2. This shows the consistence of both methods.

3.3.2. Eastern Equatorial Pacific

In the EE region, a westward propagation of the zonal velocity anomalies at semiannual (~ 200 days) periods with a wavelength of 60° , a phase speed of 0.38 m s^{-1} , and an amplitude close to 6 cm s^{-1} is observed (Figure 10a). Meridional velocity anomalies also have a westward phase propagation (0.39 m s^{-1}), but at intra-annual period (30 days) and with a wavelength of $1,000 \text{ km}$ (Figure 10b). This signal shows an

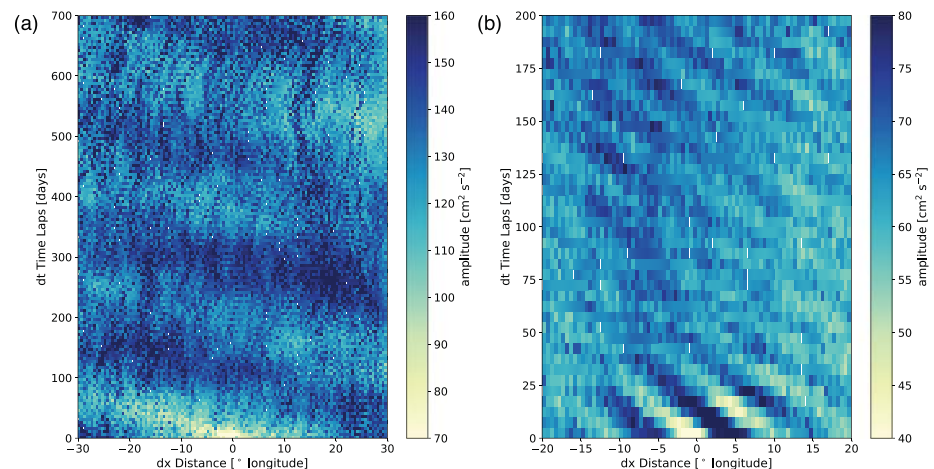


Figure 10. Same as Figure 9 in the box EE.

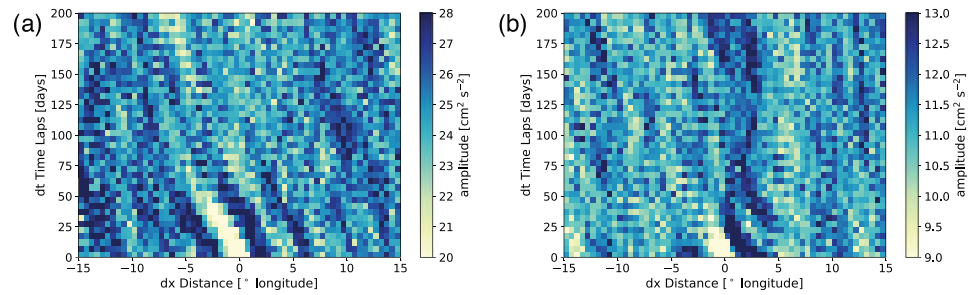


Figure 11. Same as Figure 9 for V' only in (a) TN and (b) TS.

amplitude of $\sim 4.5 \text{ cm s}^{-1}$ and a strong phase coherence over at least 20° and 300 days. It is, however, modulated by a low-frequency annual cycle (Figure 8b shows an intensification at the end of 2016 and beginning of 2017, during boreal winter time).

3.3.3. North Tropical Pacific

In the TN region, a westward propagation of meridional velocity anomalies with phase speed around 0.09 m s^{-1} is observed (Figure 11a). It is associated with periods of 70 days and wavelengths of $\sim 500 \text{ km}$. The $\text{SSF}_{V'}$ has an amplitude of $\sim 30 \text{ cm}^2 \text{ s}^{-2}$, which corresponds to anomalies of amplitude $\sim 3 \text{ cm s}^{-1}$. The signal loses coherence at $dt > 100$ days and $dx > 10^\circ$.

3.3.4. South Tropical Pacific

The $\text{SSF}_{V'}$ in the TS region shares features with the TN region, including a westward propagation with phase speed around 0.09 m s^{-1} (Figure 11b) and similar scales (periods of 70 days and wavelengths of $\sim 500 \text{ km}$). Its amplitude ($14 \text{ cm}^2 \text{ s}^{-2}$) is, however, much weaker than in the TN region, as already evidenced from Figure 4c, and the phase decoherence occurs at shorter scales. This suggests that although they are energetically important, the waves or eddies associated with these patterns are very transient and localized, which makes them difficult to capture.

3.3.5. Pacific Western Boundary

In the WB region, we performed SSF in the x and in the y directions, but no particular patterns have been found. This can result from the fact that many different scales are present and superimposed.

3.3.6. Conclusions

In summary, the variability associated with U' is intensified in the equatorial band and is found on large scales (annual and semiannual periods with wavelengths of the order of the basin scale). The variability associated with V' is found at the equator and north of the equator at shorter scales (periods smaller than 70 days and wavelengths smaller than $1,000 \text{ km}$) (Table 2).

Table 2

Summary of Characteristic Scales Found in Each Region Defined in Figure 4 for the Zonal Velocity (U), the Meridional Velocity (V), and the Zonal Velocity Minus the Seasonal Cycle (U^*)

		U'					V'					U^* T (day)
		T (day)	λ (km)	A (cm s^{-1})	c_ϕ (m s^{-1})	M (-)	T (day)	λ (km)	A (cm s^{-1})	c_ϕ (m s^{-1})	M (-)	
●	EE	180	$\sim 6,000$	6.3	0.38	$\leq 3.10^{-3}$	30	$\sim 1,000$	4.5	0.39	7.10^{-2}	120
●	EW	360	$\sim 15,000$	10	0.5	$\leq 5.10^{-3}$	50	750	3.5	0.2	1.10^{-1}	120
●	TN	360	–	–	–	–	70	500	3	0.09	2.10^{-1}	70
●	TS	360	–	–	–	–	70	500	1.5	0.09	1.10^{-1}	–
●	WB	360	–	–	–	–	~ 60	–	–	–	–	~ 80

Note. The seasonal cycle is mostly present in the 5°S to 5°N band; U^* is thus computed for the EE and EW regions only. T is the period, λ the wavelength, A the amplitude, c_ϕ the phase speed, and $M = \frac{Ak^2}{\beta}$, where $k = \frac{2\pi}{\lambda}$ is the wavenumber (equivalent meridional wavenumber for U' and zonal wavenumber for V'). Note that the equivalent meridional wavenumber can only be overestimated such that M for U' is an upper bound. β is the meridional gradient of the Coriolis parameter, a nondimensional parameter that measures the nonlinearity of the flow. $M \ll 1$ indicates a weak nonlinearity (the variability can be associated with waves) and $M \gg 1$ indicates a strong nonlinearity (the variability can be associated with eddies).

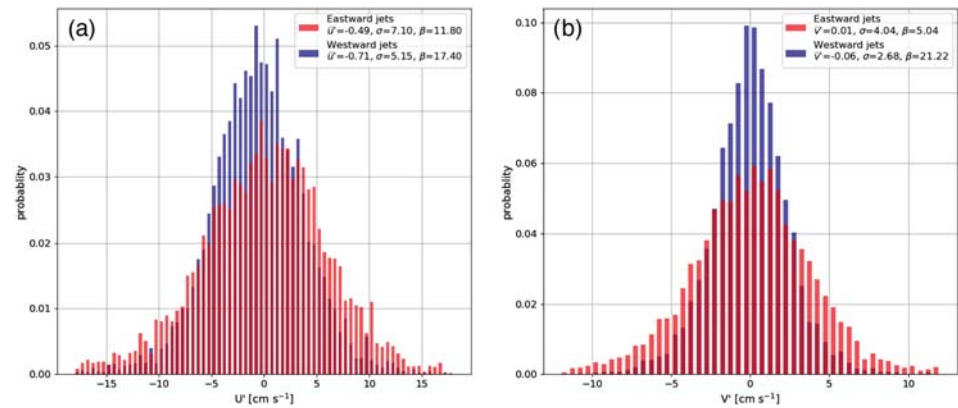


Figure 12. Statistics of (a) \bar{U}' and (b) \bar{V}' in eastward jets (red histograms) and westward jets (blue histograms). Histograms are normalized such that the integral over the range is 1. They represent the probability density function at the bin. Statistical indicators are given in the legend. \bar{U}' , \bar{V}' are velocity fluctuation averages, σ standard deviation, and β kurtosis.

3.4. Strengthening of EKE at the Jet Scale

The aim of this section is to better document the characteristics of the maxima of EKE found in eastward jets (Figure 5). The method used in the previous sections to estimate the period and wavelength associated with the EKE relies on statistical approaches within large regions (sections 2.2.2 and 2.2.3). Therefore, it cannot be applied at such a small scale as the jets scale. The approach here is to document and quantify the possible origin of this meridional distribution of EKE.

Distributions of zonal and meridional velocity anomalies, U and V , are unimodal in eastward and westward jets (Figure 12). The standard deviation σ measures the spread of the distribution values. Eastward jets have higher σ (7.1 and 4 for U' and V') than westward jets (5.2 and 2.7 for U' and V'). So velocities reach more frequently extreme values in eastward jets. The eastward to westward standard deviation ratio for V' ($\sigma_e/\sigma_w = 1.5$) is stronger than for U ($\sigma_e/\sigma_w = 1.3$), showing a stronger signature of the variability in V' than in U' . In addition, this variability is also associated with a strong signature in EAPE: Figure 13 shows local maxima of EAPE inside eastward jets, showing that the jet-scale EKE is associated with strong isopycnal fluctuations. All these results suggest the presence of waves or eddies intensified locally inside the eastward jets.

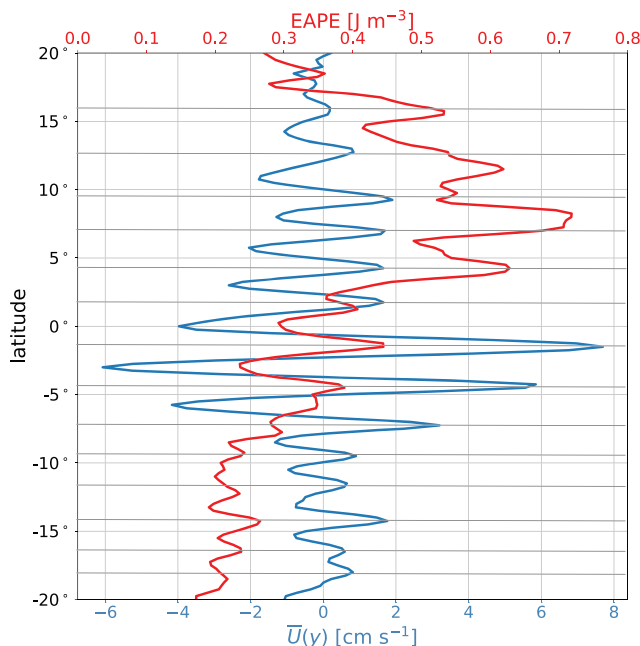


Figure 13. Mean zonal velocity $\bar{U}(y)$ (blue) and eddy available potential energy (EAPE) (red) at 1,000 m averaged from 180° to 120°W.

The jet-scale intensified EKE can be generated either locally (through instability of the mean flow for example) or remotely and reach these depths and regions through propagation. For geostrophic flows, barotropic instability occurs when the gradient of potential vorticity changes sign within an isopycnal layer. In this case, the condition can be approximated by a change of sign of $-\partial_{yy}\bar{U} + \beta$, where β is the meridional gradient of the Coriolis parameter (Cushman-Roisin & Beckers, 2011; Drazin & Howard, 1966; Rayleigh, 1879). In the jets, this condition is almost never satisfied, except possibly in the westward jet near 3°S (Figure 14a). The mean circulation is stable to barotropic perturbations. We thus do not expect the MKE to transfer energy to the EKE locally. The EKE has to come from a remote energy source or other physical processes, such as baroclinic instability.

Conversely, the EKE can have a local effect on the mean flow. The $-\bar{U}\partial_y \bar{U}'\bar{V}'$ term acts as a source term in the MKE budget (e.g., Capó et al., 2019; Gula et al., 2016). This term is found to be predominantly positive within 7° of the equator (Figure 14b), revealing a transfer of energy from EKE to

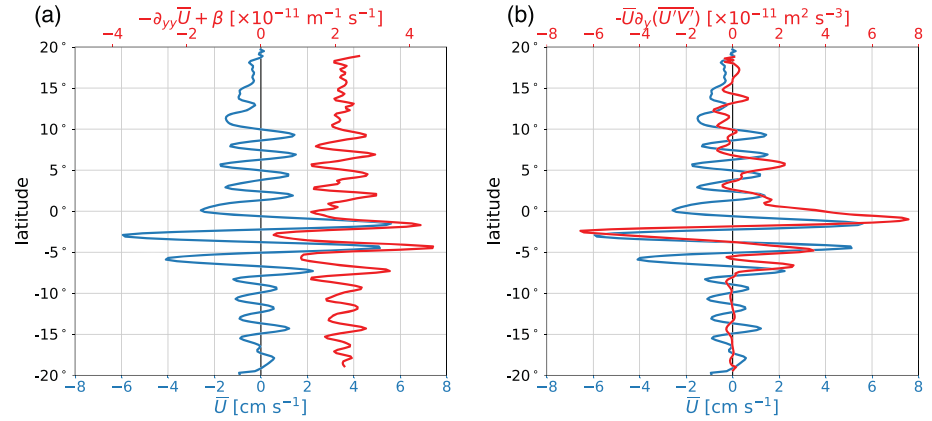


Figure 14. Mean zonal velocity $\bar{U}(y)$ (blue) and (a) barotropic instability criterion (red); (b) production term in the MKE budget that corresponds to EKE→MKE energy transfer (red) at 1,000 m averaged from 180° to 120°W.

MKE except in the jet near 3°S ($-\bar{U}\partial_y\bar{U}'\bar{V}' < 0$), where barotropic instability can be active in transferring MKE to EKE (Figure 14a). The amplitude of the EKE to MKE transfer is roughly $2.10^{-11} \text{ m}^2 \text{ s}^{-3}$. Given the amplitude of the MKE ($2.5 \times 10^{-3} \text{ m}^2 \text{ s}^{-2}$ based on a 5 cm s^{-1} mean velocity \bar{U}), the time scale for the EKE to significantly impact the MKE is of order 1,000 days, which should remain shorter than the dissipative time scale. In the next section, a potential mechanism that is compatible with the idea of energy transfer from EKE to the mean flow is discussed.

4. Summary and Discussion

Generally zonal velocities are found to vary on large temporal and spatial scales, from semi-annual to annual periods and several thousands of kilometers (Table 2) with a large amplitude that accounts for 64% of the total kinetic energy (not shown). The meridional velocities are found to vary on much shorter temporal

and spatial scales at intra-annual periods (30–100 days) and few hundreds of kilometers. When annual variability is filtered out, the zonal velocities also exhibit intra-annual periods, compatible with the meridional velocities off the equator. The EKE is also larger close to the equator and tends to decrease poleward, although local maxima are observed, especially in the northern part of the basin.

4.1. Waves Propagation and Possible Generation Mechanisms

The aim of this section is to examine how the observed EKE can be consistent with the signature of propagating planetary waves and to discuss their possible generation mechanisms.

We define the nondimensional parameter M as

$$M = \frac{Ak^2}{\beta} \quad (14)$$

where A is the amplitude of the variability in zonal or meridional velocity, k its meridional or zonal wavenumber, and β the meridional gradient of the Coriolis parameter. M is a measure of the nonlinearity of planetary flows (e.g., Gill, 1974). $M \ll 1$ indicates quasilinear flow and $M \gg 1$ indicates nonlinear flow. This parameter is computed in each region using the characteristics found from the scale analysis (Table 2). Note that for U' , the equivalent

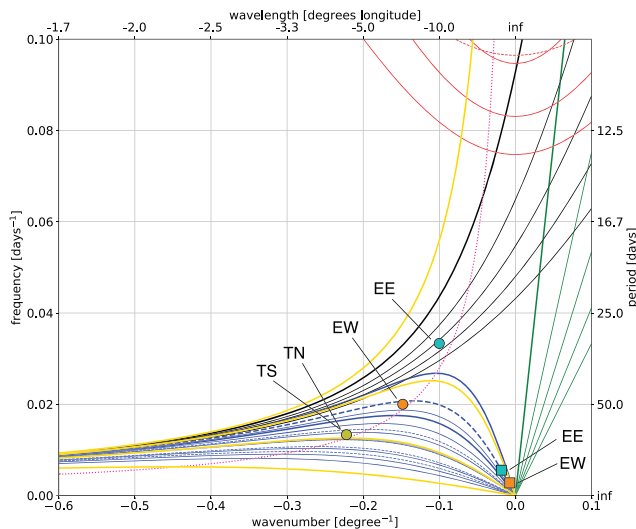


Figure 15. Dispersion relation for equatorially trapped and barotropic Rossby waves for a realistic basin-averaged stratification from the climatology CARS (Ridgway & Dunn, 2007). Green: Kelvin waves. Black: Yanai waves. Red: inertia-gravity waves. Blue: Rossby waves. Thick lines: first baroclinic modes. Solid lines: odd meridional modes. Dashed lines: even meridional modes. Yellow: barotropic Rossby wave dispersion relation for $k_y = 0, 10^{-6}, 2 \times 10^{-6} \text{ m}^{-1}$, and $4 \times 10^{-6} \text{ m}^{-1}$. Colored dots: (k, ω) for V' from estimation in the different regions (Table 2). Colored squares: same for U' .

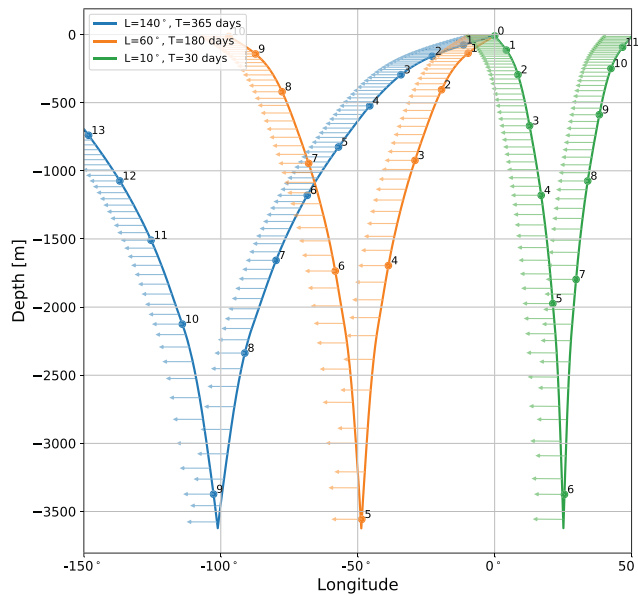


Figure 16. Ray tracing of equatorial Rossby waves of meridional mode 1 with an annual period (blue line) and semiannual period (orange line) and of a Yanai wave of period of 30 days (green line) initially generated at the surface. The lines indicate the vertical propagation of the energy, they are graduated with a scale of 1 month (dots), and the arrows indicate the phase speed of the wave. The stratification is taken from the climatology CARS (Ridgway & Dunn, 2007) averaged over the entire tropical Pacific.

meridional wave scale is taken as the latitude range length of the regions in which the SSF is applied and can be underestimated. In all regions, $M < 10^{-1}$. This suggests that the deep EKE footprint is more likely to be associated with linear waves than with nonlinear eddies. The different scales signature for EKE_U and EKE_V can result from the different KE signature of equatorial waves. Long waves have indeed higher kinetic energy (KE) associated with the zonal component of the velocity, while short waves have higher KE associated with the meridional component of the velocity.

The equatorial zonal velocity anomalies are associated with annual periods in the western part ($\sim 180^\circ$) of the basin and with semiannual periods in the eastern part ($\sim 125^\circ$). Both scales are compatible with long Rossby waves dispersion relation (Figure 15). The east-west difference can be explained by the vertical propagation of the energy associated with equatorial Rossby waves of annual and semiannual periods. Annual Rossby waves have a shallower ray path and reach 1,000 m at about 70° west of their generation site (Figure 16). If they are generated close to the eastern boundary by reflection of wind-generated equatorial Kelvin waves (as suggested by White, 1977), they are expected to reach 1,000 m around 180° , as observed in the western part (EW). Our data also show that annual variability can be present in the middle or eastern part of the basin (Figure 7b). This is compatible with earlier observations (Cravatte et al., 2012; Kessler & McCreary, 1993) that have detected annual Rossby waves at 140°W . This could be explained by the propagation of annual Rossby waves in the presence of the mean currents (Vallis, 2017). Similarly, semiannual Rossby waves reach 1,000 m at 40° west of their generation site (Figure 16). If generated close to the eastern boundary, they are thus expected around 130°W , a longitude consistent with the one observed. This supports the idea of vertically propagating long Rossby waves generated at the surface close to the eastern boundary. The filtered equatorial zonal velocity U^* has periodic fluctuations around 75 and 120 days (Figure 7e), which are compatible with wind-driven equatorial Kelvin waves as reported from satellite altimetry and subsurface in situ data analysis (Cravatte et al., 2003).

The equatorial meridional velocity anomalies present a strong signal in the spectral range of the TIWs at 30 days, 1,000 km in the eastern part of the basin. This signal is compatible with high baroclinic mode or vertically propagating Yanai waves (Figure 15). It can be related to the downward propagation of TIWs, as evidenced from mooring observations in the Atlantic Ocean (e.g., Bunge et al., 2008; Tuchen et al., 2018; Von Schuckmann et al., 2008). The TIWs in the equatorial Pacific are also associated with periods of 17 days (Lyman et al., 2007). Although our method does not enable us to estimate periods shorter than 20 days (section 2.2.2 and Appendix A), a possible aliasing of shorter periods cannot be excluded. The phase speed of the V' propagation (Figure 10) is compatible with estimates for TIWs (Chelton et al., 2000; Willett et al., 2006). In addition, TIWs are known to be intensified at the surface from July to November (Willett et al., 2006). We observe the intensification of the deep TIW-like signal from September to February (Figure 6a). This temporal lag is consistent with the downward energy propagation time of about 3 months for Yanai waves of period of 30 days and wavelength 10° (Figure 16). All these elements support the vertical propagation of TIWs at depths of at least 1,000 m. In the western part of the basin, waves at 50-day periods and 750-km wavelengths are observed, matching the dispersion relation for second meridional and first baroclinic mode short Rossby waves (Figure 15). Although they have not been extensively mentioned in the literature, they are compatible with the observations of Bunge et al. (2008) and Tuchen et al. (2018) in the Atlantic Ocean.

The off-equatorial meridional velocity anomalies (poleward of 7°) have a dominant spectral signature at 70 days and 500 km. These spectral characteristics are compatible with the dispersion relation of barotropic Rossby waves for nonzero meridional wavenumber or high meridional and baroclinic mode Rossby waves. These characteristics are also compatible with the presence of westward-propagating eddies with diameters

of 200–250 km, which is the typical scale expected at these latitudes (Chelton et al., 2011; Yang et al., 2013). An important source of eddy generation is located along the Central American coast, where the wind form eddies of diameter around 150–300 km that propagate further west at speeds of 5–15 cm s⁻¹ (Kurczyn et al., 2012; Stumpf & Legeckis, 1977; Willett et al., 2006). The distinction on the nature (waves or eddies) of the observed anomalies at depth is not trivial. Several arguments, however, would support that these anomalies are associated with waves rather than eddies. The nonlinearity parameter is of order 10⁻¹ (Table 2), and the signal is found to be coherent over the latitudinal extent of the TN region, that is, at least 7° (Figure 11). This meridional coherence suggests large meridional scale anomalies. This is compatible with the presence of barotropic Rossby waves, which are not equatorially trapped and can have large meridional extent. Farrar (2011) noted the presence of barotropic Rossby waves radiating from the TIWs and reaching 20°. However, the period and wavelength he measured are not compatible with those observed here. The question of the origin of these waves remains. Some evidence of waves generated by barotropic and baroclinic instabilities of surface currents is given by Farrar and Weller (2006) from observations at 10°N, 125°W, in the tropical Pacific and by Tchilibou (2018) from a realistic mesoscale resolving simulation of the tropical Pacific. In the latter study, the author shows that in the north tropical Pacific, the shear and density gradient between the westward NEC and the eastward Subtropical Countercurrent (STCC) and Hawaiian Lee Countercurrent (HLCC) (Figure 1) generate barotropic and baroclinic instabilities. A spectral energy budget shows that baroclinic instability produces EKE at intra-seasonal periods (close to 50 days) and short wavelengths (300 km). Barotropic instability is smaller but produces EKE at 100-day periods and 400-km wavelengths.

4.2. A Link with the Formation and Maintenance of the Mean Jet-Structured Circulation

Our study gives some insight into the possible origin of the mean deep circulation, with its alternating zonal jets. The maxima of meridional variability (Figure 5b) and EAPE (Figure 13) in eastward jets are inconsistent with the eddy-averaging hypothesis (Berloff et al., 2011), which would lead to maxima between the jets. Several studies have shown that waves, and in particular short intra-annual waves, are a possible energy source for the mean deep equatorial circulation. They efficiently propagate energy downward because of their steep ray paths (Cox, 1980) and they are prone to instabilities that develop jet-like structures (Hua et al., 2008; Ménesguen et al., 2009). Forcing a numerical simulation with a wave maker of 50-day period at the equator, Ménesguen et al. (2009) were able to reproduce the near-equatorial jets within the 3°S to 3°N latitude range. Similarly, Ascani et al. (2010) were able to reproduce meridionally alternating jet-like structures in the near-equatorial band by forcing a vertically propagating Yanai wave beam at 30-day period and 1,000-km wavelength. The short waves (periods <100 days and wavelengths <1,000 km) observed in this study at the equator and off the equator at 1,000-m depth give some observational evidence for the energy sources required by this mechanism.

The modulation of the EKE and EAPE intensity at the jet scale with higher EKE and EAPE inside eastward jets is compatible with a process called “jet sharpening” that might help maintain these jets (Dritschel & McIntyre, 2008; Dritschel & Scott, 2011). The presence of the jets leads to a modification of the background potential vorticity gradient, shaped as a staircase profile with fronts inside eastward jets (Delpech et al., 2020). The jet-sharpening theory predicts that these potential vorticity staircases will modify the Rossby elasticity and favor a wave regime inside the eastward jets (as Rossby waves need a potential vorticity gradient to propagate) and a turbulent regime inside westward jets. This dual regime maintains the potential vorticity staircases and thus the jets themselves. Therefore, we can expect the wave dynamical signal to be intensified in regions of strong potential vorticity gradients. The Argo observations provide a 10-day low-pass filtered EKE that will more likely capture the wave regime than the high-frequency turbulent mixing. The observations of higher EKE and EAPE within eastward jets (Figures 5 and 13) are thus consistent with the jet-sharpening theory. Another consequence of the presence of jets and varying background potential vorticity gradients is the local modification of the phase speed of the wave. This deforms wave fronts and can create a convergence of energy flux (Greatbatch et al., 2018) and a transfer of energy towards the mean flow (MKE), as evidenced from Figure 14b.

To conclude, observations of intensified EKE and APE along eastward jets are consistent with a variability associated with propagating Rossby waves whose structure is locally modified by the deep jet structure. They can also possibly support the jet-sharpening mechanism. These results remain qualitative, and a full

understanding of the mechanisms would require numerical simulations that are beyond the scope of this study.

4.3. Perspectives

This study provides the first basin-scale description of the 1,000-m EKE, from Lagrangian float displacements. Although the analysis of this unique database has provided new insight into the spatial and temporal variability of currents at 1,000 m, it is, like all observational analyses, limited by the characteristics of the observations.

One limitation arises from the temporal and spatial sampling of the Argo drifts. During the 2014–2018 period when sampling was most frequent, there were an average of 10 measurements per square degree per year. To retain robust statistics, we were unable to choose a region that is too narrow as this limits the number of measurements. For this reason, the scale analysis could not be refined to characterize the scales of energy in small localized regions (as inside jets). However, the increasing number of floats over time and the recommendation of doubling Argo density in the equatorial ocean (Smith et al., 2019) should allow higher resolution in future studies.

Another limitation is imposed by the quasi-Lagrangian nature of the Argo drift velocities. Ideally, a systematic method to correct the Doppler shift would allow us to estimate the wavenumber and frequency of the EKE with a good precision for each float and would thus provide a local information about the different scales of variability, as well as their spatial and temporal variations. Such corrections are, however, not straightforward and often require strong assumptions (Barbot et al., 2018). No appropriate method exists to date, and this would deserve a full investigation in future studies.

Finally, although the methodology developed in this study has been applied to provide a description of the spectral content at 1,000-m depth only, it will hopefully be useful to investigate the energy scale dependence at other depths. In particular, a comparison with the scale dependence of surface variability, using for example drifters velocities, in combination with theoretical energy ray tracing would help in determining which part of the observed deep spectrum is surface driven and which part is internally driven. In addition, a more thorough analysis of the vertical energy propagation using the EAPE at the different depths would be valuable as an attempt to address the question of the vertical energy propagation in the equatorial regions.

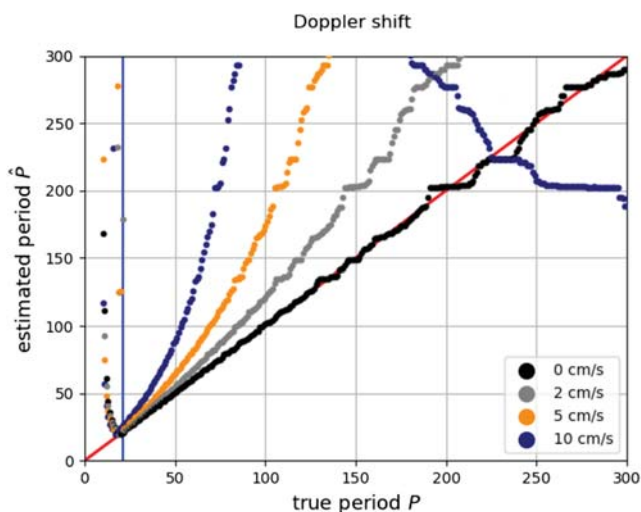


Figure A1. Period estimated by the wavelet analysis method as a function of the true period. The velocity time series are reconstructed following the Argo protocol: the float is advected with a high-resolution Eulerian velocity field, the trajectory is subsampled at a 10-day sampling period, and the velocity time series is reconstructed from the differential float positions. Each color corresponds to a background mean flow velocity amplitude. The wave has a wavelength of 1,000 km. The blue line indicates the period corresponding to the Nyquist frequency, and the red line indicates the first bisector $y = x$ where the estimated period fits the true period.

Appendix A: Wavelet Analysis Validation: Doppler Shift Influence on Period Estimation

The purpose of this appendix is to quantify the error made on the estimation of the period by neglecting the Doppler shift. We perform experiments with a single synthetic float. The synthetic float is advected in a prescribed wave field with a background mean flow. The positions of the float are then subsampled every 10 days along its trajectory, and the velocities are estimated using the differential positions to reconstruct an Argo-like data set. The period of the wave is then estimated by performing a wavelet analysis on the float velocity time series. The estimated period (\hat{P}) is then compared with the true period of the wave (P) for different waves and background mean flow velocities.

For all the experiments, we consider a plane wave propagating along the zonal direction with a wavenumber k and a frequency ω and a zonal background mean flow \bar{u}_0 . The float is thus advected in the Eulerian velocity field given by Equation A1:

$$\{ u = \bar{u}_0, v = v_0 \sin(kx - \omega t) \} \quad (\text{A1})$$

A first experiment with $\bar{u}_0 = 0$ shows that every period larger than the period corresponding to the Nyquist frequency can be estimated with very little error (Figure A1). There is little influence of taking the 10-day

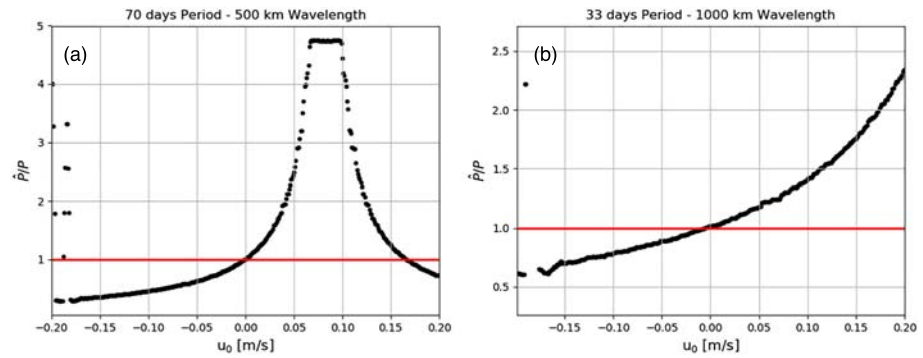


Figure A2. Ratio of estimated period to the true period as a function of the mean zonal velocity u_0 for a (a) wave (70 days, 500 km, $c_\varphi = 0.08$) and (b) TIW-like wave (33 days, 1,000 km, $c_\varphi = 0.35$). The red line corresponds to a ratio of 1 where the estimated period fits the true period. A maximum of the error on the estimated period is reached when the velocity u_0 matches the phase speed of the wave.

averaged velocities as instantaneous velocities and the Lagrangian time series as a Eulerian time series. This ensures that the method described in section 2.2.2 is valid in spite of the two first approximations made.

Three other experiments with $\overline{u_0} = 2, 4, \text{ and } 6 \text{ cm s}^{-1}$ are performed. In practice, the deep mean flow in the tropical oceans is mainly zonal and does not exceed $6\text{--}8 \text{ cm s}^{-1}$ (e.g., Figure 5). These experiments are thus representative of realistic conditions. The wave period is estimated with a greater error compared to the true period as the background mean flow velocity increases. The error increases also with the period and depends on the wavelength.

More generally, the error increases as the background mean velocity approaches the phase speed of the wave (Figure A2). The error is “linear” with the velocity sign: for positive wave phase speed, a positive background mean flow leads to an overestimation of the wave period and a negative background mean flow leads to underestimation of the wave period. For high phase speed waves (Figure A2b), the error remains small (because the mean flow will never reach the phase speed), and when periods are averaged over a region large enough to encompass both eastward and westward jets, the individual error might compensate and give a good estimate for the period. For low phase speed waves, however, the error can be as large as the wave period. In this study, it has been checked that the wave phase speeds are always large compared to the mean currents, so that the calculated periods are reliable.

Appendix B: Statistical Scale Function Validation

The purpose of this appendix is to validate the statistical method developed in section 2.2.3 to infer wave properties (period, wavelength, and amplitude) from random velocity measurements at depth. We perform experiments with synthetic floats within a prescribed wave field. We numerically advect 50 synthetic floats during 3 years with random start dates and positions in an idealized wave velocity field with a superimposed zonal current given by Equation B1. The float positions are subsampled every 10 days along the trajectories.

$$\{ u = \overline{u_0} + v_0 \sin(kx - \omega t) \} v = v_0 \cos(kx - \omega t) \quad (\text{B1})$$

where k is the wavenumber, ω the period, and v_0 the amplitude of the wave. The background mean flow is set to $\overline{u_0} = 5 \text{ cm s}^{-1}$. The velocity are estimated using the differential positions in order to reconstruct an Argo-like data set (U_{syn}, V_{syn}). The $SSF_{U_{syn}}$ and $SSF_{V_{syn}}$ are then computed as described in section 2.2.3.

Two experiments with a period of 70 days, a wavelength of 500 km, and amplitudes of 3 (Figure B1a) and 10 cm s^{-1} (Figure B1b) are tested. In Figure B1, only the $SSF_{V_{syn}}$ is shown, but the $SSF_{U_{syn}}$ is identical.

The period and wavelength of the wave are estimated with a good precision. In particular, this method is not sensitive to the Doppler shift (even in the case where the amplitude of the wave is small compared to the background current). As expected, the amplitude of the SSF varies with the amplitude of the wave. However, the estimated amplitude (2.5 cm s^{-1} for the first experiment and 7 cm s^{-1} for the second one) is

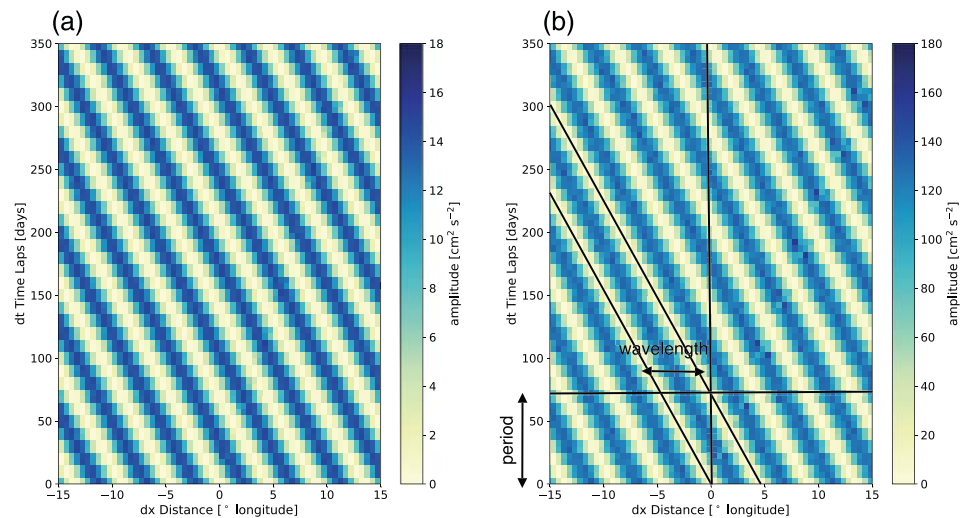


Figure B1. SSF for synthetic floats in an analytical wave field of period of 70 days, wavelength 500 km, and amplitudes of (a) 3 and (b) 10 cm s^{-1} .

slightly underestimated. This can be due to the 10-day average resulting from the data set construction (Lebedev et al., 2007). This average acts as a boxcar low-pass filter that can yield significant attenuation, even for frequency a bit lower than the filter length. The SSF is therefore a very powerful tool to measure the spectral signature of the signal provided by the Argo floats, although the amplitudes estimated from the SSF can be underestimated.

Data Availability Statement

This study used the data of YoMaHA07 (Lebedev et al., 2007) data set of velocities derived from Argo float trajectories provided by APDRC/IPRC, available at <https://apdrc.soest.hawaii.edu/projects/yomaha/> (last accessed 09/04/2020). The EAPE data set is available at <https://www.seanoe.org/data/00612/72432/> (last accessed: 09/04/2020).

Acknowledgments

The authors are grateful to G. Roulet who provided the EAPE data set. This work benefited from fruitful discussions with G. Serazin, M. Tchilibou, S. Barbot, and J. Gula. The authors are also grateful to N. Hall for the grammatical corrections and to E. Firing and one anonymous reviewer for their insightful comments that have improved the quality of the manuscript.

References

- Ascani, F., Firing, E., Dutrieux, P., McCreary, J. P., & Ishida, A. (2010). Deep equatorial ocean circulation induced by a forced-dissipated Yanai beam. *Journal of Physical Oceanography*, *40*(5), 1118–1142.
- Ascani, F., Firing, E., McCreary, J. P., Brandt, P., & Greatbatch, R. J. (2015). The deep equatorial ocean circulation in wind-forced numerical solutions. *Journal of Physical Oceanography*, *45*(6), 1709–1734.
- Babiano, A., Basdevant, C., & Sadourny, R. (1985). Structure functions and dispersion laws in two-dimensional turbulence. *Journal of the Atmospheric Sciences*, *42*(9), 941–949.
- Balwada, D., LaCasce, J. H., & Speer, K. G. (2016). Scale-dependent distribution of kinetic energy from surface drifters in the Gulf of Mexico. *Geophysical Research Letters*, *43*, 10,856–10,863. <https://doi.org/10.1002/2016GL069405>
- Barbot, S., Petrenko, A., & Maes, C. (2018). Intermediate water flows in the western south Pacific: As revealed by individual Argo floats trajectories and a model re-analysis. *Biogeosciences*, *15*(13), 4103–4124. <https://doi.org/10.5194/bg-15-4103-2018>
- Bastin, S., Claus, M., Brandt, P., & Greatbatch, R. J. (2020). Equatorial deep jets and their influence on the mean equatorial circulation in an idealized ocean model forced by intraseasonal momentum flux convergence. *Geophysical Research Letters*, *47*, e2020GL087808. <https://doi.org/10.1029/2020GL087808>
- Berloff, P., Karabasov, S., Farrar, J. T., & Kamenkovich, I. (2011). On latency of multiple zonal jets in the oceans. *Journal of Fluid Mechanics*, *686*, 534–567.
- Bunge, L., Provost, C., Hua, B. L., & Kartavtseff, A. (2008). Variability at intermediate depths at the equator in the Atlantic Ocean in 2000–06: Annual cycle, equatorial deep jets, and intraseasonal meridional velocity fluctuations. *Journal of Physical Oceanography*, *38*(8), 1794–1806.
- Capó, E., Orfila, A., Mason, E., & Ruiz, S. (2019). Energy conversion routes in the western Mediterranean Sea estimated from eddy-mean flow interactions. *Journal of Physical Oceanography*, *49*(1), 247–267.
- Chelton, D. B., Schlax, M. G., & Samelson, R. M. (2011). Global observations of nonlinear mesoscale eddies. *Progress in Oceanography*, *91*(2), 167–216.
- Chelton, D. B., Wentz, F. J., Gentemann, C. L., de Szoeke, R. A., & Schlax, M. G. (2000). Satellite microwave SST observations of transequatorial tropical instability waves. *Geophysical Research Letters*, *27*(9), 1239–1242.
- Contreras, R. F. (2002). Long-term observations of tropical instability waves. *Journal of Physical Oceanography*, *32*(9), 2715–2722.

- Cox, M. D. (1980). Generation and propagation of 30-day waves in a numerical model of the Pacific. *Journal of Physical Oceanography*, *10*(8), 1168–1186.
- Cravatte, S., Kessler, W. S., & Marin, F. (2012). Intermediate zonal jets in the tropical Pacific Ocean observed by Argo floats. *Journal of Physical Oceanography*, *42*(9), 1475–1485.
- Cravatte, S., Kestenare, E., Marin, F., Dutrieux, P., & Firing, E. (2017). Subthermocline and intermediate zonal currents in the tropical Pacific Ocean: Paths and vertical structure. *Journal of Physical Oceanography*, *47*(9), 2305–2324.
- Cravatte, S., Picaut, J., & Eldin, G. (2003). Second and first baroclinic Kelvin modes in the equatorial Pacific at intraseasonal timescales. *Journal of Geophysical Research*, *108*(C8), 3266. <https://doi.org/10.1029/2002JC001511>
- Cushman-Roisin, B., & Beckers, J.-M. (2011). *Introduction to geophysical fluid dynamics: Physical and numerical aspects*: Academic Press.
- Delpech, A., Cravatte, S., Marin, F., Morel, Y., Gronchi, E., & Kestenare, E. (2020). Observed tracer fields structuration by middepth zonal jets in the tropical Pacific. *Journal of Physical Oceanography*, *50*(2), 281–304. <https://doi.org/10.1175/JPO-D-19-0132.1>
- Drazin, P. G., & Howard, L. N. (1966). Hydrodynamic stability of parallel flow of inviscid fluid, *Advances in applied mechanics* (Vol. 9, pp. 1–89). Elsevier.
- Dritschel, D. G., & McIntyre, M. E. (2008). Multiple jets as pV staircases: The Phillips effect and the resilience of eddy-transport barriers. *Journal of the Atmospheric Sciences*, *65*(3), 855–874.
- Dritschel, D. G., & Scott, R. K. (2011). Jet sharpening by turbulent mixing. *Philosophical Transactions of the Royal Society A: Mathematical, Physical and Engineering Sciences*, *369*(1937), 754–770.
- Eriksen, C. C., & Richman, J. G. (1988). An estimate of equatorial wave energy flux at 9- to 90-day periods in the central Pacific. *Journal of Geophysical Research*, *93*(C12), 15,455–15,466.
- Farrar, J. T. (2011). Barotropic Rossby waves radiating from tropical instability waves in the Pacific Ocean. *Journal of Physical Oceanography*, *41*(6), 1160–1181.
- Farrar, J. T., & Durland, T. S. (2012). Wavenumber-frequency spectra of inertia-gravity and mixed Rossby-gravity waves in the equatorial Pacific Ocean. *Journal of Physical Oceanography*, *42*(11), 1859–1881.
- Farrar, J. T., & Weller, R. A. (2006). Intraseasonal variability near 10 N in the eastern tropical Pacific Ocean. *Journal of Geophysical Research*, *111*, C05015. <https://doi.org/10.1029/2005JC002989>
- Firing, E., Kashino, Y., & Hacker, P. (2005). Energetic subthermocline currents observed east of Mindanao. *Deep Sea Research Part II: Topical Studies in Oceanography*, *52*(3–4), 605–613.
- Gill, A. E. (1974). The stability of planetary waves on an infinite beta-plane. *Geophysical and Astrophysical Fluid Dynamics*, *6*(1), 29–47.
- Gouriou, Y., Delcroix, T., & Eldin, G. (2006). Upper and intermediate circulation in the western equatorial Pacific Ocean in October 1999 and April 2000. *Geophysical Research Letters*, *33*, L10603. <https://doi.org/10.1029/2006GL025941>
- Greatbatch, R. J., Claus, M., Brandt, P., Matthießen, J.-D., Tuchen, F. P., Ascani, F., et al. (2018). Evidence for the maintenance of slowly varying equatorial currents by intraseasonal variability. *Geophysical Research Letters*, *45*, 1923–1929. <https://doi.org/10.1002/2017GL076662>
- Gula, J., Molemaker, M. J., & McWilliams, J. C. (2016). Topographic generation of submesoscale centrifugal instability and energy dissipation. *Nature Communications*, *7*(1), 1–7.
- Hua, B. L., D'Orgeville, M., Fruman, M. D., Menesguen, C., Schopp, R., Klein, P., & Sasaki, H. (2008). Destabilization of mixed Rossby gravity waves and the formation of equatorial zonal jets. *Journal of Fluid Mechanics*, *610*, 311–341.
- Kessler, W. S., & McCreary, J. P. (1993). The annual wind-driven Rossby wave in the subthermocline equatorial Pacific. *Journal of Physical Oceanography*, *23*(6), 1192–1207.
- Kurczyn, J. A., Beier, E., Lavin, M. F., & Chaigneau, A. (2012). Mesoscale eddies in the northeastern Pacific tropical-subtropical transition zone: Statistical characterization from satellite altimetry. *Journal of Geophysical Research*, *117*, C10021. <https://doi.org/10.1029/2012JC007970>
- Lagerloef, G. S. E., Mitchum, G. T., Lukas, R. B., & Niiler, P. P. (1999). Tropical Pacific near-surface currents estimated from altimeter, wind, and drifter data. *Journal of Geophysical Research*, *104*(C10), 23,313–23,326.
- Lebedev, K. V., Yoshinari, H., Maximenko, N. A., & Hacker, P. W. (2007). Velocity data assessed from trajectories of Argo floats at parking level and at the sea surface.
- Lee, G., Gommers, R., Waselewski, F., Wohlfahrt, K., & OLeary, A. (2019). PyWavelets: A Python package for wavelet analysis. *Journal of Open Source Software*, *4*(36), 1237.
- Legeckis, R. (1977). Long waves in the eastern equatorial Pacific Ocean: A view from a geostationary satellite. *Science*, *197*(4309), 1179–1181.
- Lindstrom, E., Bourassa, M., Chelton, D., Corlett, G., Durland, T., Farrar, T., et al. (2014). White paper# 9—Satellite views of the tropical Pacific.
- Lukas, R., & Firing, E. (1985). The annual Rossby wave in the central equatorial Pacific Ocean. *Journal of Physical Oceanography*, *15*(1), 55–67.
- Lyman, J. M., Chelton, D. B., DeSzoeke, R. A., & Samelson, R. M. (2005). Tropical instability waves as a resonance between equatorial Rossby waves. *Journal of Physical Oceanography*, *35*(2), 232–254.
- Lyman, J. M., Johnson, G. C., & Kessler, W. S. (2007). Distinct 17- and 33-day tropical instability waves in subsurface observations. *Journal of Physical Oceanography*, *37*(4), 855–872.
- Marin, F., Kestenare, E., Delcroix, T., Durand, F., Cravatte, S., Eldin, G., & Bourdalle-Badie, R. (2010). Annual reversal of the equatorial intermediate current in the Pacific: Observations and model diagnostics. *Journal of Physical Oceanography*, *40*(5), 915–933.
- McCaffrey, K., Fox-Kemper, B., & Forget, G. (2015). Estimates of ocean macroturbulence: Structure function and spectral slope from Argo profiling floats. *Journal of Physical Oceanography*, *45*(7), 1773–1793.
- McPhaden, M. J. (1996). Monthly period oscillations in the Pacific north equatorial countercurrent. *Journal of Geophysical Research*, *101*(C3), 6337–6359.
- Menesguen, C., Delpech, A., Marin, F., Cravatte, S., Schopp, R., & Morel, Y. (2019). Observations and mechanisms for the formation of deep equatorial and tropical circulation. *Earth and Space Science*, *6*, 370–386. <https://doi.org/10.1029/2018EA000438>
- Menesguen, C., Hua, B. L., Fruman, M. D., & Schopp, R. (2009). Dynamics of the combined extra-equatorial and equatorial deep jets in the Atlantic. *Journal of Marine Research*, *67*(3), 323–346.
- Morel, P., & Larcheveque, M. A. (1974). Relative dispersion of constant level balloons in the 200 mb general circulation. *Journal of Atmospheric Sciences*, *31*, 2189–2196.
- Ollitrault, M., & Colin de Verdière, A. (2014). The ocean general circulation near 1000-m depth. *Journal of Physical Oceanography*, *44*(1), 384–409.

- Ollitrault, M., Lankhorst, M., Fratantoni, D., Richardson, P., & Zenk, W. (2006). Zonal intermediate currents in the equatorial Atlantic Ocean. *Geophysical Research Letters*, *33*, L05605. <https://doi.org/10.1029/2005GL025368>
- Ollitrault, M., & Rannou, J.-P. (2013). ANDRO: An Argo-based deep displacement dataset. *Journal of Atmospheric and Oceanic Technology*, *30*(4), 759–788.
- Philander, S. G. H. (1978). Instabilities of zonal equatorial currents, 2. *Journal of Geophysical Research*, *83*(C7), 3679–3682.
- Qiu, B., Rudnick, D. L., Chen, S., & Kashino, Y. (2013). Quasi-stationary north equatorial undercurrent jets across the tropical north Pacific Ocean. *Geophysical Research Letters*, *40*, 2183–2187. <https://doi.org/10.1002/grl.50394>
- Rayleigh, L. (1879). On the stability, or instability, of certain fluid motions. *Proceedings of the London Mathematical Society*, *1*(1), 57–72.
- Ridgway, K. R., & Dunn, J. R. (2007). Observational evidence for a Southern Hemisphere oceanic supergyre. *Geophysical Research Letters*, *34*, L13612. <https://doi.org/10.1029/2007GL030392>
- Roemmich, D., Alford, M. H., Claustre, H., Johnson, K., King, B., Moum, J., et al. (2019). On the future of Argo: A global, full-depth, multi-disciplinary array. *Frontiers in Marine Science*, *6*(439). <https://doi.org/10.3389/fmars.2019.00439>
- Roulet, G. (2020). World ocean atlas of Argo inferred statistics. <https://doi.org/10.17882/72432>
- Roulet, G., Capet, X., & Maze, G. (2014). Global interior eddy available potential energy diagnosed from Argo floats. *Geophysical Research Letters*, *41*, 1651–1656. <https://doi.org/10.1002/2013GL059004>
- Sérazin, G., Marin, F., Gourdeau, L., Cravatte, S., Morrow, R., & Dabat, M.-L. (2020). Scale-dependent analysis of in situ observations in the mesoscale to submesoscale range around New Caledonia. *Ocean Science Discussions*, *2019*, 1–32. <https://doi.org/10.5194/os-2019-124>
- Smith, N., Kessler, W. S., Cravatte, S., Sprintall, J., Wijffels, S., Cronin, M. F., et al. (2019). Tropical Pacific observing system. *Frontiers in Marine Science*, *6*, 31. <https://doi.org/10.3389/fmars.2019.00031>
- Stumpf, H. G., & Legeckis, R. V. (1977). Satellite observations of mesoscale eddy dynamics in the eastern tropical Pacific Ocean. *Journal of Physical Oceanography*, *7*(5), 648–658.
- Tchilibou, M. L. (2018). Dynamique méso-sous-mésoséchelle et marée interne dans le pacifique tropical: Implications pour l'altimétrie et la mer des salomon (Ph.D. Thesis).
- Torrence, C., & Compo, G. P. (1998). A practical guide to wavelet analysis. *Bulletin of the American Meteorological Society*, *79*(1), 61–78.
- Tuchen, F. P., Brandt, P., Claus, M., & Hummels, R. (2018). Deep intraseasonal variability in the central equatorial Atlantic. *Journal of Physical Oceanography*, *48*(12), 2851–2865.
- Vallis, G. K. (2017). *Atmospheric and oceanic fluid dynamics*: Cambridge University Press.
- Von Schuckmann, K., Brandt, P., & Eden, C. (2008). Generation of tropical instability waves in the Atlantic Ocean. *Journal of Geophysical Research*, *113*, C08034. <https://doi.org/10.1029/2007JC004712>
- Wang, F., Li, Y., & Wang, J. (2016). Intraseasonal variability of the surface zonal currents in the western tropical Pacific Ocean: Characteristics and mechanisms. *Journal of Physical Oceanography*, *46*(12), 3639–3660.
- Weber, J. E. H. (2017). Equatorial Stokes drift and Rossby rip currents. *Journal of Geophysical Research: Oceans*, *122*, 4819–4828. <https://doi.org/10.1002/2016JC012653>
- White, W. B. (1977). Annual forcing of baroclinic long waves in the tropical north Pacific Ocean. *Journal of Physical Oceanography*, *7*(1), 50–61.
- Willett, C. S., Leben, R. R., & Lavín, M. F. (2006). Eddies and tropical instability waves in the eastern tropical Pacific: A review. *Progress in Oceanography*, *69*(2-4), 218–238.
- Wyrtki, K., & Kilonsky, B. (1984). Mean water and current structure during the Hawaii-to-Tahiti shuttle experiment. *Journal of Physical Oceanography*, *14*(2), 242–254.
- Yang, G., Wang, F., Li, Y., & Lin, P. (2013). Mesoscale eddies in the northwestern subtropical Pacific Ocean: Statistical characteristics and three-dimensional structures. *Journal of Geophysical Research: Oceans*, *118*, 1906–1925. <https://doi.org/10.1002/jgrc.20164>
- Zanowski, H., Johnson, G. C., & Lyman, J. M. (2019). Equatorial Pacific 1,000-dbar velocity and isotherm displacements from Argo data: Beyond the mean and seasonal cycle. *Journal of Geophysical Research: Oceans*, *124*, 7873–7882. <https://doi.org/10.1029/2019JC015032>
- Zhang, Z., Pratt, L. J., Wang, F., Wang, J., & Tan, S. (2020). Intermediate intraseasonal variability in the western tropical Pacific Ocean: Meridional distribution of equatorial Rossby waves influenced by a tilted boundary. *Journal of Physical Oceanography*, *50*(4), 921–933.